IRAQI JOURNAL OF APPLIED PHYSICS

The *Iraqi Journal of Applied Physics (IJAP)* is a peer reviewed journal of high quality devoted to the publication of original research papers from applied physics and their broad range of applications. IJAP publishes quality original research papers, comprehensive review articles, survey articles, book reviews, dissertation abstracts in physics and its applications in the broadest sense. It is intended that the journal may act as an interdisciplinary forum for Physics and its applications. Innovative applications and material that brings together diverse areas of Physics are particularly welcome. Review articles in selected areas are published from time to time. It aims to disseminate knowledge; provide a learned reference in the field; and establish channels of communication between academic and research experts, policy makers and executives in industry, commerce and investment institutions. IJAP is a quarterly specialized periodical dedicated to publishing original papers, letters and reviews in: Applied & Nonlinear Optics, Applied Mechanics & Thermodynamics, Digital & Optical Communications, Electronic Materials & Devices, Laser Physics & Applications, Plasma Physics & Applications, Quantum Physics & Spectroscopy, Semiconductors & Optoelectronics, Solid State Physics & Applications, Alternative and Renewable Energy, and Computers and Networks.

ISSN (Print): 1813-2065, ISSN (Online): 2309-1673, ISSN (Letters): 1999-656X

EDITORIAL BOARD

Editorial Office:
P. O. Box 55259, Baghdad 12001, IRAQ
Website: www.iraqiphysicsjournal.com
Emails: info@iraqiphysicsjournal.com, editor_ijap@yahoo.co.uk, editor@ijaponline.com

ADVISORY BOARD

SPONSORED AND PUBLISHED BY
THE IRAQI SOCIETY FOR ALTERNATIVE AND RENEWABLE ENERGY SOURCES & TECHNIQUES (I.S.A.R.E.S.T.)

IRAQI JOURNAL OF APPLIED PHYSICS

ISSN (Print): 1813-2065, ISSN (Online): 2309-1673, ISSN (Letters): 1999-656X

" INSTRUCTIONS TO AUTHORS "

CONTRIBUTIONS

Contributions to be published in this journal should be original research works, i.e., those not already published or submitted for publication elsewhere, individual papers or letters to editor.
Manuscripts should be submitted to the editor at the mailing address:
Iraqi Journal of Applied Physics, Editorial Board, P. O. Box 55259, Baghdad 12001, IRAQ
Website: www.iraqiphysicsjournal.com
Email: editor@iraqiphysicsjournal.com, editor_ijap@yahoo.co.uk

MANUSCRIPTS

Two hard copies with soft copy on a compact disc (CD) should be submitted to Editor in the following configuration:

- **One-column** Double-spaced one-side A4 size with 2.5 cm margins of all sides
- Times New Roman font (16pt bold for title, 14pt bold for names, 12pt bold for headings, 12pt regular for text)
- Letters should not exceed 10 pages, papers should not exceed 20 pages and reviews are up to author.
- Manuscripts presented in English only are accepted.
- English abstract not exceed 150 words
- 4 keywords (at least) should be maintained on (PACS preferred)
- Author(s) should express all quantities in SI units
- Equations should be written in equation form (*italic* and symbolic)
- Figures and Tables should be separated from text
- Figures and diagrams can be submitted in colors for assessment and they will be returned to authors after provide printable copies
- Charts should be indicated by the software used for
- Only original or high-resolution scanner photos are accepted
- For electronic submission, articles should be formatted with MS-Word software.

AUTHOR NAMES AND AFFILIATIONS

It is IJAP policy that all those who have participated significantly in the technical aspects of a paper be recognized as co-authors or cited in the acknowledgments. In the case of a paper with more than one author, correspondence concerning the paper will be sent to the first author unless staff is advised otherwise.
Author name should consist of first name, middle initial, last name. The author affiliation should consist of the following, as applicable, in the order noted:
- Company or college (with department name or company division), Postal address, City, state, zip code, Country name, contacting telephone, and e-mail

REFERENCES

The references should be brought at the end of the article, and numbered in the order of their appearance in the paper. The reference list should be cited in accordance with the following examples:
[1] X. Ning and M.R. Lovell, "On the Sliding Friction Characteristics of Unidirectional Continuous FRP Composites", *ASME J. Tribol.*, 124(1) (2002) 5-13.
[2] M. Barnes, "Stresses in Solenoids", *J. Appl. Phys.*, 48(5) (2001) 2000–2008.
[3] J. Jones, **"Contact Mechanics"**, Cambridge University Press (Cambridge, UK) (2000), Ch.6, p.56.
[4] Y. Lee, S.A. Korpela and R. Horne, "Structure of Multi-Cellular Natural Convection in a Tall Vertical Annulus", Proc. 7th International Heat Transfer Conference, U. Grigul et al., eds., Hemisphere (Washington DC), 2 (1982) 221–226.
[5] M. Hashish, "Waterjet Technology Development", High Pressure Technology, PVP-Vol. 406 (2000) 135-140.
[6] D.W. Watson, "Thermodynamic Analysis", ASME Paper No. 97-GT-288 (1997).
[7] C.Y. Tung, "Evaporative Heat Transfer in the Contact Line of a Mixture", Ph.D. thesis, Rensselaer Polytechnic Institute, Troy, NY (1982).

PROOFS

Authors will receive proofs of papers and are requested to return one corrected hard copy with a WORD copy on a compact disc (CD). New materials inserted in the original text without Editor permission may cause rejection of paper.

COPYRIGHT FORM

Author(s) will be asked to transfer copyrights of the article to the Journal soon after acceptance of it. This will ensure the widest possible dissemination of information.

OFFPRINTS

Authors will receive offprints free of charge and any additional reprints can be ordered.

SUBSCRIPTION AND ORDERS

Annual fees (4 issues per year) of subscription are:
50 US$ for individuals inside Iraq; **200** US$ for institutions inside Iraq;
100 US$ for individuals abroad; **300** US$ for institutions abroad.
Fees are reduced by 25% for I.S.A.R.E.S.T. members. Orders of issues can be submitted by contacting the editor-in-chief or editorial office at admin@iraqiphysicsjournal.com, or editor_ijap@yahoo.co.uk to maintain the address of issue delivery and payment way.

IRAQI JOURNAL OF APPLIED PHYSICS
Vol. 17, No. 3, July-September 2021, pp. 3-8

Preparation and Characterization of Dysprosium-Doped Titanium Dioxide Photocatalyst by Sol-Gel Method

Karim A. Abbas
Naseer F. Hasan
Riyadh M. Abood

Department of Laser and Optoelectronics Technology, Al-Furat Al-Awsat Technical University, Najaf, IRAQ

In this work, the dysprosium-doped titanium dioxide nanostructures were prepared by sol-gel method and characterized as photocatalysts for environmental applications. The morphology, composition, particle size, surface area and energy band gap of the prepared samples were studied. The effect of dysprosium ions on the photocatalytic properties of the prepared titanium dioxide nanostructures was studied and analyzed by the photocatalytic decomposition of potassium permanganate in aqueous slurry.

Keywords: Titania; Dysprosium ions; Sol-gel method; Photocatalytic activity

1. Introduction

The effect of grain size on the thermoluminescent sensitivities of dosimeter materials was first reported and studied for LiF, and later it was studied on doped $CaSO_4$ [1-4]. It was proved an increasing thermoluminescent sensitivity with the increasing grain size up to 0.5 mm grain size, and they ascribed the improved sensitivity to the higher dysprosium (Dy) concentration [5]. It was also reported that reducing the grain size by mechanical grinding did not lower the thermoluminescent response, therefore the conditions of the nucleation, especially the Dy concentrations of the solutions were found to be a determinant factor [6]. The experiments proved that the grain size effect is smaller for Tm-doped $CaSO_4$ than for Dy-doped material [7]. Furthermore, the medium grain size fractions had the highest thermoluminescent sensitivity, which seems to be in contradiction with the supposed diffusion-controlled mechanism of the crystallization [8,9].

Titanium dioxide is one of the most widely studied semi-conducting photocatalyst for the degradation of organic contaminants from water and air, because of its physical and chemical stability, high catalytic activity, high oxidative power, low cost and ease of production [10-13].

TiO_2 exists naturally as rutile, anatase, brookite and amorphous. Anatase TiO_2 has excellent photocatalytic activity [14]. There are different routes that can be used to synthesize TiO_2 such as chemical precipitation method, chemical vapour deposition (CVD) [15,16], hydrothermal method and sol-gel technique for the synthesis high quality powders, of high purity, homogeneity and controlled morphology [17,18].

Due to its high chemical stability, low toxicity and excellent electrical and optical properties, titanium dioxide (TiO_2) is the target of intense research for many applications that span from catalytic applications (photocatalysis and water splitting) to opto- and photoelectronic devices (LEDs and solar cells) [2]. In particular, TiO_2 is considered to be an excellent host for light emission applications in the visible and infrared, due to its wide optical bandgap (3.0 eV for rutile, 3.2 eV for anatase), wide transparency range and large refractive index (~2.5-3.0). Furthermore, the relatively low phonon energy of TiO_2 (<700 cm^{-1}) makes it especially suitable for the incorporation of optically active rare-earth ions such as Er^{3+} [4]. The low phonon energy is necessary to prevent fast non-radiative de-excitations of the rare-earth ions through the phonons of the matrix, thus allowing to achieve high luminescence quantum yields required to light amplifiers, LEDs and fluorophores. Interestingly, doping of TiO_2 with a few percent of rare-earth ions (La^{3+}, Pr^{3+}, Nd^{3+}, Eu^3, Gd^{3+}, Tb^{3+}, Dy^{3+}, Er^{3+}) has been also studied for a very different aim, since it has been shown that this incorporation is a suitable procedure to stabilize the TiO_2 anatase phase, contrary to incorporations of specific materials that might induce the phase transformation, i.e. Fe:TiO_2. Particularly, for the case of lanthanide doped nanocrystalline TiO_2 xerogels produced by sol-gel, it has been shown that the rare-earth doping significantly retards the anatase-to-rutile phase transformation, stabilizes the mesoporous structure and delays the reduction of surface area of nanosized TiO_2 at high temperatures [1,3,8,11,14]. All these properties being useful for an enhanced catalysis performance. Therefore, there have been two main separate lines of investigation involving the

rare earth doping of TiO_2, one focused to the optical performance and other dedicated to the structural characterization. However, in order to develop the full potential of rare earth-doped TiO_2 colloidal nanocrystalline materials for the different envisaged applications, a good understanding and control of their structure related to its optical performance is needed.

The applications of TiO_2 photocatalyst have been reported in various environmental applications such as hydrogen generation, bacteria inactivation and photocatalytic degradation [10]. Enhancement photocatalytic of TiO_2 can be achieved by doping with metals and non-metals, such Ag, SO_4^{-2} and N [19-21]. Doping lanthanide ion into TiO_2 has attracted much attention because of their unique *4f* electronic configuration and spectral characteristics, and is a method to shift the maximum of absorption spectrum as well as to enhance the photocatalytic activity [22,23].

In this work, the effect of Dy^{+3} doping concentration on the structural characteristics of TiO_2 nanostructures prepared by sol-gel method is introduced in order to investigate the effect of such dopants on the TiO_2 photocatalytic activity.

2. Experimental Work

Titanium isopropoxide (TIP, 97%, Aldrich) is used as precursor for Titania. At first, TIP and deionized water are mixed together in terms of Ti: H_2O molar ratio 0f 0.00289. Acetic acid is used to adjust the pH environment and for restrain the hydrolysis reaction of the solution. The solution is then vigorously stirred for 1 hour and subsequently ultrasonicated for 15 min in ice bath in order to form sol. After aging at 70°C for 12 hour, the sol phase is transformed into gel. In order to obtain TiO_2 nanoparticles, the gel is dried at 100°C and then sintered at 450°C for 3 hour and subsequently powdered to obtain desired TiO_2nanocrystalline. For the Dy^{+3} doping, dysprosium chloride ($DyCl_3.H_2O$), from sigma- Aldrich, is dissolved in ethanol solution at different Dy^{+3} concentrations; 0.018, 0.037, 0.053, 0.083, and 0.119 %. In each recipe, 0.5 ml of ($DyCl_3.H_2O$) solution is added to the TIP-H_2O mixture and the pH value of the final mixture is normalized to be 3. The nanoparticles suspend as films using spin coating process. Figure (1) shows a schematic diagram of the experimental steps.

The photocatalytic activity of undoped TiO_2 and Dy-doped samples was investigated by measuring the photodegradation efficiency of Potassium permanganate ($KMnO_4$) dye solution with concentration of 2×10^{-5} [M] as a pollutant model. Different prepared samples were placed in this solution and then the samples were placed in a UV light exposure cabinet in which they were illuminated with (18 W) UV-source of range (200-400) nm and (17W) VIS-source (Xe arc lamp) of range (250-600) nm at a distance of (5 cm) from the substrates. The incident visible radiation from this lamp was filtered with HOYA UV 385 cutoff filter to eliminate light in the UV region.

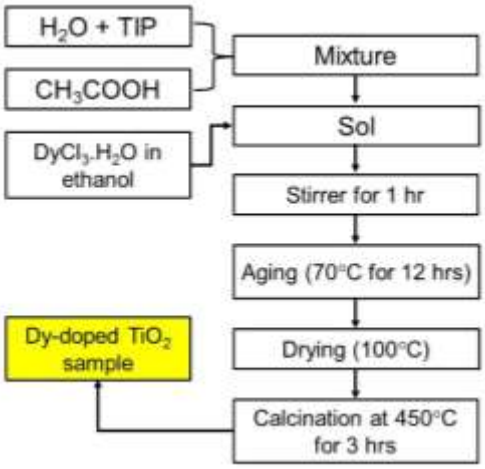

Fig. (1) Schematic diagram of the preparation of Dy-doped TiO_2 photocatalyst

3. Results and Discussion

The x-ray diffraction (XRD) patterns of the prepared samples are shown in Fig. (2). The anatase phase of TiO_2 is observed, through the peaks at 2θ of 25.5, 37.8, 48.2, 53.5 and 55 degree, for all prepared samples and can be obtained by controlling the annealing temperature. No other polymorph of Titania is observed and no dysprosium peaks are found in the XRD patterns. This may give primary indication that the doping process with Dy^{+3} did not change the structural phase of TiO_2.

From the line broadening of the corresponding XRD peaks and using the Scherer's formula, the crystallite size (D) is estimated by [24]

$$D=K\lambda/(\beta\cos\theta) \quad (1)$$

where λ is the wavelength of the x-ray radiation (0.154056 nm for Cu-lamp); K is a constant usually taken as 0.9; and β is the full-width at half-maximum (FWHM) in radians, and θ is the diffracting angles

The broadening of diffraction peaks indicates small size of nanocrystals (see table 1). The crystallite size was calculated for the diffraction plane (101) and was found to be slightly decreased with increasing of Dy^{+3} concentrations as compared with undoped TiO_2 sample. Also, the unit cell parameters *a* and *c* were slightly increased with the content of Dy^{+3} ions and this may give us primary indication for the possibility of incorporation of Dy^{+3} ions into the lattice of anatase.

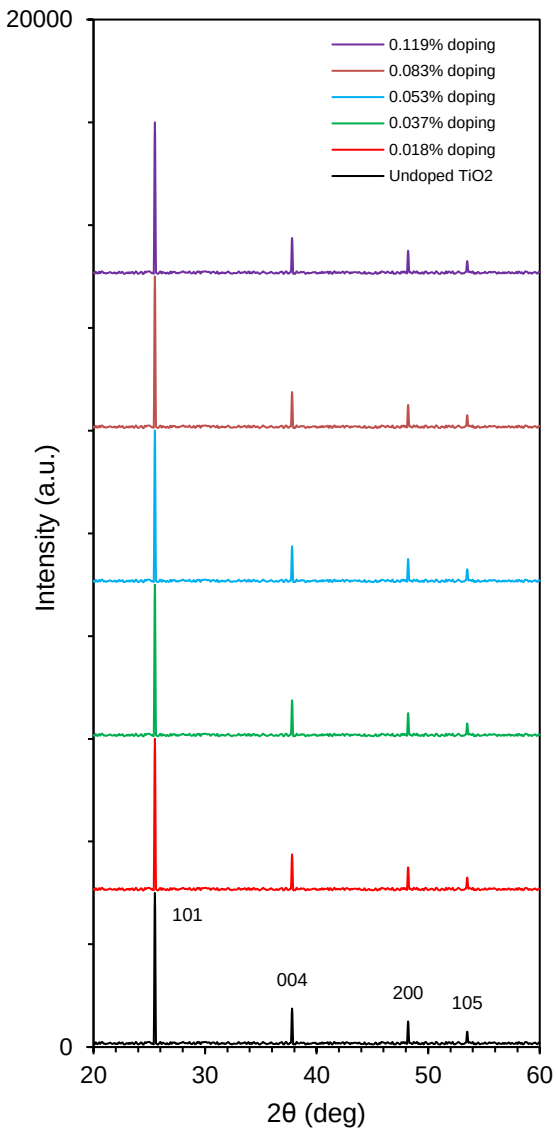

Fig. (2) XRD patterns of undoped and doped TiO_2 samples prepared in this work

Table (1) Crystallite size, unit cell parameters *a* and *c*, surface area and porosity as a function of Dy concentrations.

Sample	Dy Concent. (%)	Particle size (nm)	Cell Parameter *a*	Cell Parameter *c*
0	0.3756	15.1	-	0.9496
1	0.3788	14	0.018	0.9521
2	0.3771	12.8	0.037	0.9472
3	0.3743	10.11	0.053	0.9448
4	0.3767	9.81	0.083	0.9456
5	0.3795	9.32	0.119	0.9472

Sample	BET ($m^2.g^{-1}$)	Pore volume ($cm^3.g^{-1}$)	Pore size (nm)
0	64.38	0.17	10.61
1	69.45	0.2	9.89
2	77.01	0.25	9.5
3	83.05	0.29	8.87
4	87.33	0.315	7.68
5	96.25	0.39	7.21

BET surface area of the prepared samples has been determined from nitrogen adsorption-desorption isotherms using Micromeritices ASAP 2020 instrument. The BET method has been used for surface area, the pore volume and the pore size calculations. Figure (3) illustrates the plot of adsorption and desorption isotherms of the TiO_2 sample. This plot is matching with type IV, which characterize mesoporous adsorbent.

For lower temperatures, it shows adsorption hysteresis [25], of the six principal classes of isotherm shapes. The mesoporous structure and high BET surface area of the samples are expected to enhance adsorption of organic compounds onto the particle surface. The surface area is higher with increasing of Dy^{+3} ions and can be reduced the crystallite size of TiO_2, which also contribute to the enhancement of adsorption capacity of TiO_2 for organic pollutants [26,27].

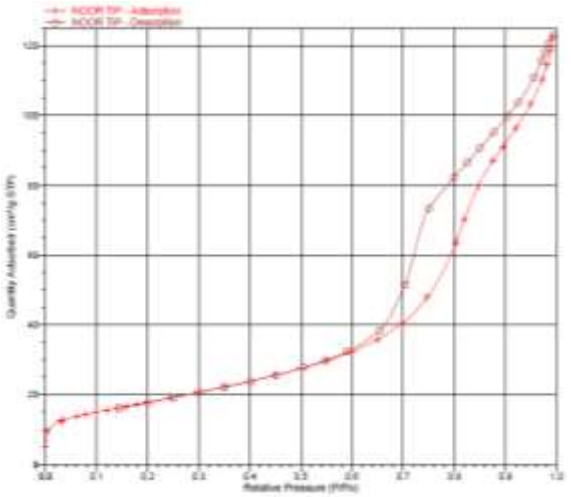

Fig. (3) Plot of adsorption and desorption isotherms of the TiO_2 sample

The absorption spectra of the prepared samples are shown in Fig. (4). The Dy^{+3}-doped TiO_2 samples obviously exhibit a visible light absorption at around (380-405) nm, whereas the absorption edge of TiO_2 sample is located at 371 nm. Therefore, the doping of TiO_2 samples with Dy^{+3} ions has significantly affected the light absorption property of the photocatalyst. This result indicates that the dopants formed an impurity band above the valence band of the TiO_2 due to the shifts in the absorption edge [28,29].

The impurity band formation can be explained by a mechanism similar to that of the NO-doped TiO_2 with cationic N species [30,31]. Red shifts of absorption edge toward the visible region were observed for the doped samples compared to undoped TiO_2. The correlation between the amount of rare earth metal and the absorption edge shift to a longer wavelength was observed. The linear absorption coefficient (α) can be expressed by the following equation [32]:

$$\alpha = A\,(h\upsilon - E_g)^n / h\upsilon \qquad (2)$$

where E_g is the absorption band gap, A is constant and n depends on the nature of the transitions. The energy band gap can be calculated using Eq. (2) and from the intercept of the tangent to the plot $(\alpha h\upsilon)^{1/2}$ versus photon energy ($h\upsilon$). It can be noticed that the values of energy band-gap are decreased with increasing content of Dy^{+3}ions.

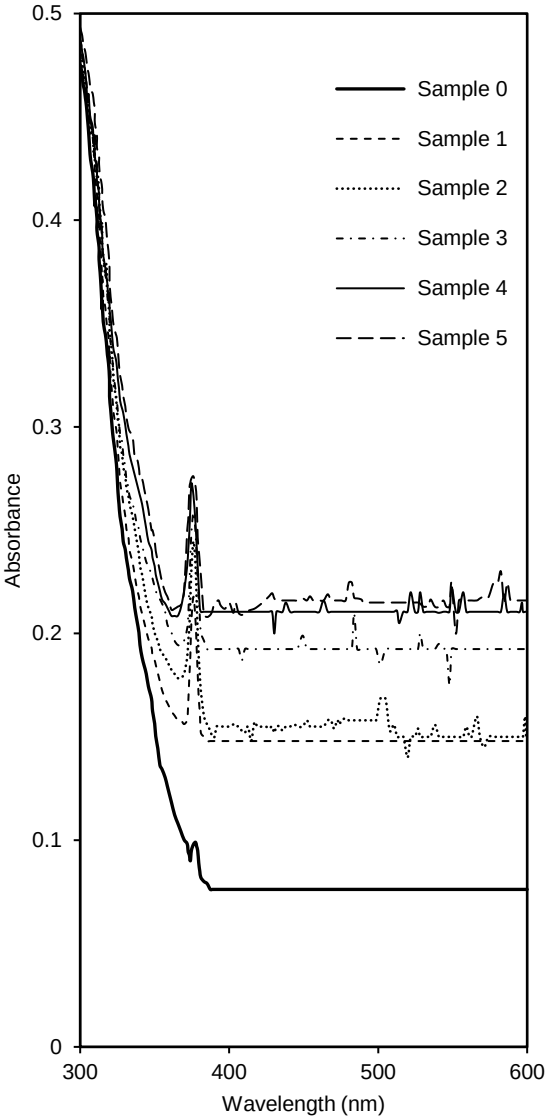

Fig. (4) Absorption spectra of the prepared samples

Table (2) Energy band gap, particle size and rate constant for the prepared samples as a function of Dy^{+3} concentrations

Sample	Energy band gap (eV)	Particle size (nm)
Sample 0	3.23	54
Sample 1	3.2	53
Sample 2	3.14	51
Sample 3	3	51
Sample 4	2.91	50
Sample 5	2.89	47

The photocatalytic efficiency of undoped TiO_2 and Dy-doped samples have been scrutinized by the photodegradation of aqueous $KMnO_4$ under UV irradiation in 75 minutes as shown in Fig. (5). It is clearly observed that the photocatalytic activity of Dy^{+3} doped TiO_2 photocatalyst is more effective, especially for doping level at 0.119 %, and also shown faster reaction comparing to other sample. The higher reactivity seems to be mostly related to the pure anatase phase of the sample and secondly with the nanometric size of the particles. These two properties have been previously pointed out as important factors for photocatalytic reactions [33].

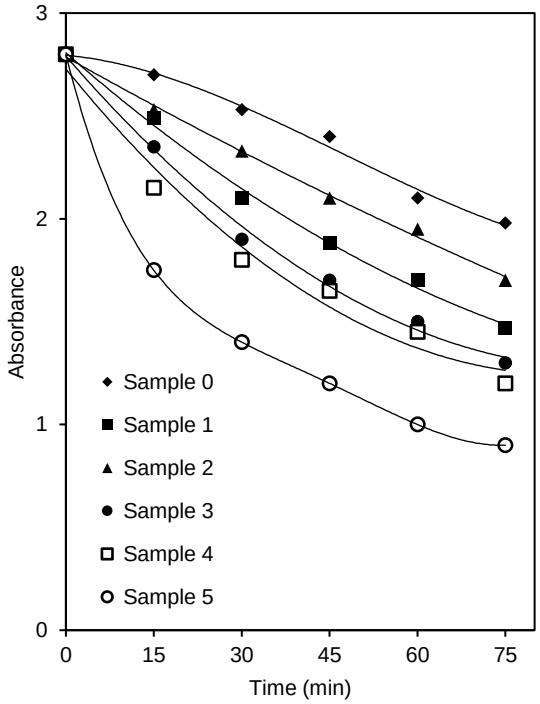

Fig. (5) Decay of absorbance of $KMnO_4$ versus UV-irradiation time for undoped and doped TiO_2 samples

The results show that the rate constant (k)-values of the degradation of ($KMnO_4$) dye for doped samples are higher than that for undoped TiO_2. The k-values are increased with the decreasing of absorbance decay (A) values of ($KMnO_4$). Hence, the photocatalytic activity can be increased as (k) values increased. Similar behavior is observed under visible irradiation in the same time (75 min.) for all prepared samples as shown in Fig. (6). The optimized sample (T5) shows a little absorbance decay, where it reached about 50% of its initial value after 75 minutes for UV irradiation, and it reached about 14% after the same time for visible irradiation.

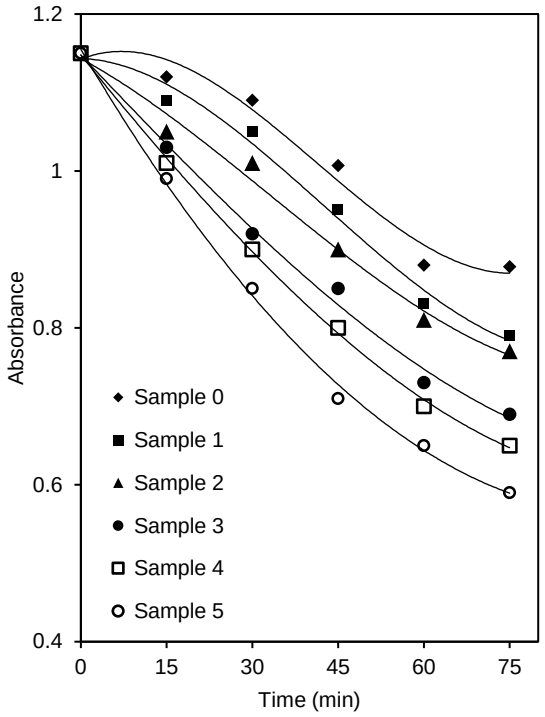

Fig. (6) Decay of absorbance of $KMnO_4$ versus visible irradiation time for undoped and doped TiO_2 samples

4. Conclusions

Thin films of different concentration of Dy^{+3} doped TiO_2 have been prepared via sol-gel technique and spin coating process. The absorption edge of anatase TiO_2 is shifted towards the visible region with the existence of Dy^{+3} ions due to the narrowing band gap of TiO_2. The efficiency of photocatalytic activity has been enhanced under UV and visible irradiations for Dy^{+3}-doped samples comparing with undoped TiO_2. The optimum concentration of Dy^{+3} has been found to be 0.119 % under irradiation in 75 minutes. The present results suggest that good performance of TiO_2 photocatalyst in visible region can be improved by Dy^{+3} ions doping.

References

[1] O.A. Hamadi, "Profiling of Antimony Diffusivity in Silicon Substrates using Laser-Induced Diffusion Technique", Iraqi J. Appl. Phys. Lett., 3(1) (2010) 23-26.

[2] 3. J. Félszerfalvi, P. P. Szabó, J. Bacsó, P. Kovács, PACT. Proc. Specialist Seminar on Thermoluminescence Dating, Oxford, UK. July 1978, Part II. (1979) 311.

[3] O.A. Hamadi, "Characterization of SiC/Si Heterojunction Fabricated by Plasma-Induced Growth of Nanostructured Silicon Carbide Layer on Silicon Surface", Iraqi J. Appl. Phys., 12(2) (2016) 9-13.

[4] A.R. Lakshmanan, S. S. Shinde, R. C. Bhatt, S. J. Supe, Radiat. Prot. Dosim., 22(3) (1988) 173.

[5] O.A. Hamadi, B.A.M. Bader and A.K. Yousif, "Electrical Characteristics of Silicon p-n Junction Solar Cells Produced by Plasma-Assisted Matrix Etching Technique", Eng. Technol. J., 28 (2008).

[6] I. Kása, Periodica Polytechnica, 28(3-4) (1984) 251.

[7] O.A. Hammadi, "Production of Nanopowders from Physical Vapor Deposited Films on Nonmetallic Substrates by Conjunctional Freezing-Assisted Ultrasonic Extraction Method", Proc. IMechE, Part N, J. Nanomater. Nanoeng. Nanosys., 232(4) (2018) 135-140.

[8] I. Kása, Radiat. Prot. Dosim., 33(1-4) (1990) 299-302.

[9] O.A. Hammadi, M.K. Khalaf, F.J. Kadhim, "Fabrication of UV Photodetector from NiO Nanoparticles Deposited on Silicon Substrate by CFUBDM Sputtering Technique", Opt. Quantum Electron., 47(12) (2015) 3805-3813.

[10] A. Fujishima, T.N. Rao and D.A. Tryk, "Titanium dioxide photocatalysis", J. Photochem. Photobio. C, 1(1) (2000) 21.

[11] M.R. Hoffmann et al., "Environmental Applications of Semiconductor Photocatalysis", Chem. Rev., 95 (1995) 69-96.

[12] A. Fujishima and K. Honda, "Electrochemical Photolysis of Water at a Semiconductor Electrode", Nature, 238 (1972) 37-38.

[13] T. Hisanga, K. Harada and K. Tanaka, "Photocatalytic degradation of Organochlorine compounds in suspended TiO_2", J. Photochem. Photobiol. A, 54 (1990) 113-118.

[14] S. Mahshid et al., "Mixed-phase TiO_2 nanoparticles preparation using sol–gel method", J. Alloys and Comp., 47 (2009) 586-589.

[15] S. Mashid et al., "Synthesis of TiO_2 nanoparticles by hydrolysis and peptization of tittaniumisopropoxide solution", Semicond. Phys., Quantum Electron. Optoelectron., 9 (2006) 65-68.

[16] S. Jian and W. Xudong, "Growth of rutile titanium dioxide nanowires by pulsed chemical vapour deposition", Cryst. Growth Des., 11 (2011) 949-954.

[17] J.-K. Oh et al., "Synthesis of phase-and shape controlled TiO_2 nanoparticles via hydrothermal process", J. Indust. Eng. Chem., 15 (2009) 270-274.

[18] M. Kanna and S. Wongnawa, "Mixed Amorphous and Nanocrystalline TiO_2 Powders Prepared by Sol-Gel Method: Characterization and Photocatalytic Study", Mater. Chem. Phys., 110 (2008) 166-175.

[19] M.K. Seery et al., "Silver doped titanium dioxide nanomaterials for enhanced visible light photocatalysis", J. Photochem. Photobio. A, 189 (2007) 258-263.

[20] H. Nishikiori, M. Hayashibe and T. Fujii, "Visible Light-Photocatalytic Activity of Sulfate-Doped Titanium Dioxide Prepared by the Sol−Gel Method", Catalysts, 3 (2013) 363-377.

[21] W. Mekprasart et al., "Effect of Nitrogen Doping on Optical and Photocatalytic Properties of TiO_2 Thin

Film Prepared by Spin Coating Process", Energy Procedia, 34 (2013) 746-750.
[22] Z. Zhao and Q. Liu, "Effects of lanthanide doping on electronic structures and optical properties of anatase TiO_2 from density functional theory calculation", J. Phys. D: Appl. Phys., 41 (2008) 085417.
[23] M.S. Hassan et al., "TiO_2nanofibers doped with rare earth elements and their photocatalytic activity", Ceram. Int., 38 (2012) 5925-5930.
[24] Y. Zhang et al., "Synthesis and electro chemical studies of a layered spherical TiO_2 through low temperature solvothermal method", Electro. Acta, 54 (2009) 4079-4083.
[25] S.J. Gregg and K.S.W. Sing, **"Adsorption, Surface Area and Porosity"**, Academic Press (London, 1982), 42-84.
[26] C.-H. Liang et al., "The effect of erbium on the adsorption and photodegradation of orange I in aqueous Er^{3+}-TiO_2 suspension", J. Hazard. Mater., 138 (2006) 471-478.
[27] C.-H. Liang et al., "The effect of praseodymium on the adsorption and photocatalytic degradation of azo dye in aqueous Pr^{3+}-TiO_2 suspension", Chem. Eng. J., 147 (2009) 219-225.
[28] K. Balachandran, R. Venckatesh and R. Sivaraj, "Synthesis of Nano TiO_2-SiO_2 composite using sol-gel method: Effect of size, surface morphology and thermal stability", Int. J. Eng. Sci. Technol., 2(8) (2010) 3695-3700.
[29] D. Chatterjee and S. Dasgupta, "Visible light induced photocatalytic degradation of organic pollutants", J. Photochem. Photobiol. C, 6 (2005) 186-205.
[30] Y. Yokosuka et al., "Photocatalytic degradation of trichloroethylene using N-doped TiO_2 prepared by a simple sol-gel process", Res. Chem. Intermed, 35 (2009) 43-53.
[31] H. Nishikiori et al., "Nitrogen doping into titanium dioxide by the sol-gel method using nitric acid", Res. Chem. Intermed., 37 (2011) 869-881.
[32] Y. Zhao et al., "Synthesis and Optical Properties of TiO_2 Nanoparticles", Mater. Lett., 61 (2007) 79-83.
[33] A.J. Maira et al., "Fourier Transform Infrared Study of the Performance of Nanostructured TiO_2 Particles for the Photocatalytic Oxidation of Gaseous Toluene", J. Catalysis, 202 (2001) 413-420.

IRAQI JOURNAL OF APPLIED PHYSICS
Vol. 17, No. 3, July-September 2021, pp. 9-12

Structural Characteristics of Nickel Oxide-Doped Tellurium Oxide Thin Films Prepared by Pulsed-Laser Deposition

Yasir A. Baydhon
Sally R. Kamal
George M. Sabbag

Department of Physics, College of Science, University of Damascus, Damascus, SYRIA

In this work, tellurium oxide thin films were prepared and doped with nickel oxide at different doping ratios using pulsed-laser deposition technique. The influence of doping level of tellurium oxide films with different amounts of nickel oxide additives (5, 10, 15 and 20%) on the structural characteristics of these films was studied and compared to those of pure tellurium oxide films. The x-ray diffraction patterns showed that all prepared films have polycrystalline structure with tetragonal phase for tellurium oxide and monoclinic phase for nickel oxide with no reaction between them. The surface morphology of the prepared films was analyzed and it revealed the formation of nano-size grains for tellurium oxide films doped with 10 and 15% nickel oxide.

Keywords: Tellurium oxide; Nickel oxide; Thin films; Structural properties

1. Introduction

Tellurium-dioxide (TeO) is a widely used ceramic material [1]. It has a direct band-gap which width is equal to 3.6 eV [2,3] and high exciton binding energy of 130 meV, and excellent optical and electrical properties with outstanding chemical and physical stabilities in harsh environments [4-6]. Stoichiometric TeO is an insulator, small shifts from its perfect stoichiometry (i.e. TeO_{-x}, with x<1), or shallow doping (F or Sb) lead to n-type semi-conductive behavior of the material [7,8]. Its electrical conductance results from point defect such as oxygen vacancies and interstitial tellurium atoms, that acts as donor [9,10]. For this reason, TeO is grouped with a category of materials known as transparent conductive oxides (TCOs) which combines high electrical conductivity with optical transparency [11-13]. Due to their low fabrication cost, TeO thin films have a widely application such as gas sensor materials, low-emission glasses and heat mirrors, flat panel displays, touch panels, oxidation catalysts, flexible electronics, dye-sensitized solar cells (DSSCs), etc. [14-17]. TeO is considered one of the promising candidates for constructing the short wavelength optoelectronic devices, such as ultraviolet light emitting diodes (LEDs), laser diodes solar- and visible-blind photodetectors [3,18-21].

An increased concern over safety in civilian homes and industrial settings, much attention has been paid to the search for semiconductor gas sensor [21,22]. The detection and control of H_2S which is bad smelling and toxic gas is very important in laboratories and industrial areas where it is used as process gas or generated as a byproduct [23]. H_2S gas finds many applications in fields such as auto ventilation units, and medical field of dentistry [24].

In the present study, NiO-doped TeO powders with different doping ratio were prepared by solid state reaction by using pulsed laser deposition technique. The structural properties and surface morphology of these films were investigated.

2. Experimental Details

Nickel oxide was added to TeO powder with different doping ratios (5, 10, 15, 20%) by solid state reaction using NiO (99.9% Fluke) and TeO (99.5% ERAK). The two binary compounds mixed carefully for two hours and pressed at 10 tons to form a target (pellet shape with 10 mm diameter and 2.5 mm thickness), and then sintered at 900°C for two hours.

The NiO-doped TeO thin films were deposited on glass and silicon substrates using pulsed-laser deposition (PLD) technique using the second harmonic generation (SHG) from an Nd:YAG Q-switched laser beam with pulse width of 10 ns, pulse energy of 400 mJ, and repetition frequency of 6 Hz. The laser shots (up to 400) were directed on the target surface with an angle of 45°. The experimental setup of PLD technique is schematically shown in Fig. (1).

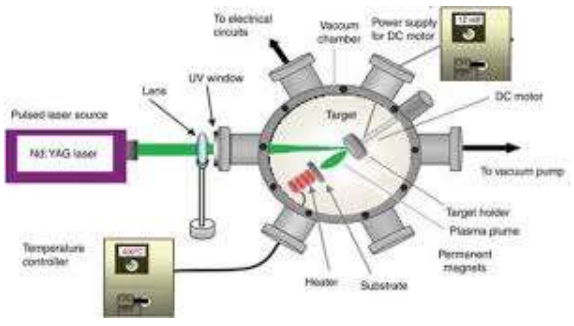

Fig. (1) Scheme of experimental setup of PLD technique

The deposition was carried out inside a chamber evacuated down to 0.01 mbar. Single crystal n-type (P-doped) silicon wafer with (111) crystal orientation, 508 μm thickness and electrical resistivity of 1.5-4 Ω.cm were used as substrates. Square shape Si samples each of 10 mm^2 area were prepared. The films should be homogenous as much as possible to ensure good quality. The crystal structure analysis of these films was examined using Miniflex II Rigaku x-ray diffractometer (XRD) with CuK_α radiation of wavelength 1.54 Å and scan angle 2θ within 20-60°. Surface morphology measurement was performed using CSPM-AA 3000 Angstrom atomic force microscope (AFM).

3. Result and Discussion

The x-ray diffraction (XRD) patterns of pure and doped TeO with (5, 10, 15, 20%) NiO films are shown in Fig. (2). It can be seen that all films have polycrystalline structure. Pure TeO exhibited sharp peaks at 2θ values of 26.56°, 33.88°, 37.98°, 51.80°, 54.72° and 57.82°, which correspond to reflections from (110), (101), (200), (211), (220) and (002) planes of tetragonal phase with preferential orientation in [110] direction.

The doped TeO film with 5% NiO shows sharp peaks at 26.58°, 33.88°, 37.98°, 51.82°, 54.76° and 57.86° which correspond to reflections from (110), (101), (200), (211)/(112), (220) and (002)/(202) planes of tetragonal phase of TeO and monoclinic phase of NiO which appear at the same position of TeO at 51.82° and 57.86°, where the intensity of these two peaks increase with doping, these peaks are in agreement with the standard values of JCPDS 96-900-7534 of TeO and 96-900-8962 of NiO.

For 10% NiO-doped TeO film, the position of peaks change to the values 26.56°, 33.88°, 37,96°, 51.78°, 54.74° and 57.9°. Also, it was changed for 15% NiO-doped TeO film to 26.56°, 33.88°, 37.96° and 51.78°. Finally, the 2θ values for 20% NiO-doped TeO film change to 26.54°, 33.86°, 38.00°, 51.82°, 54.82° and 58.06°.

The XRD patterns of the mixed films shows that the crystallinity of the films varies depending on the ratio of NiO doping in these films, where it reduced and some peaks were diminished with increase the ratio of NiO. All these result are shown in Table (1).

Table (2) Surface roughness, and r.m.s roughness, and crystalline size of pure TeO and doped with NiO films

Samples	Surface Roughness (nm)	R.M.S Roughness nm)	Average Grain Diameter (nm)
Pure TeO	7.73	9.03	115.09
5% NiO	7.59	9.11	128.16
10% NiO	5.63	6.50	61.84
5% NiO	9.52	11.0	70.25
20% NiO	11.90	13.70	119.43

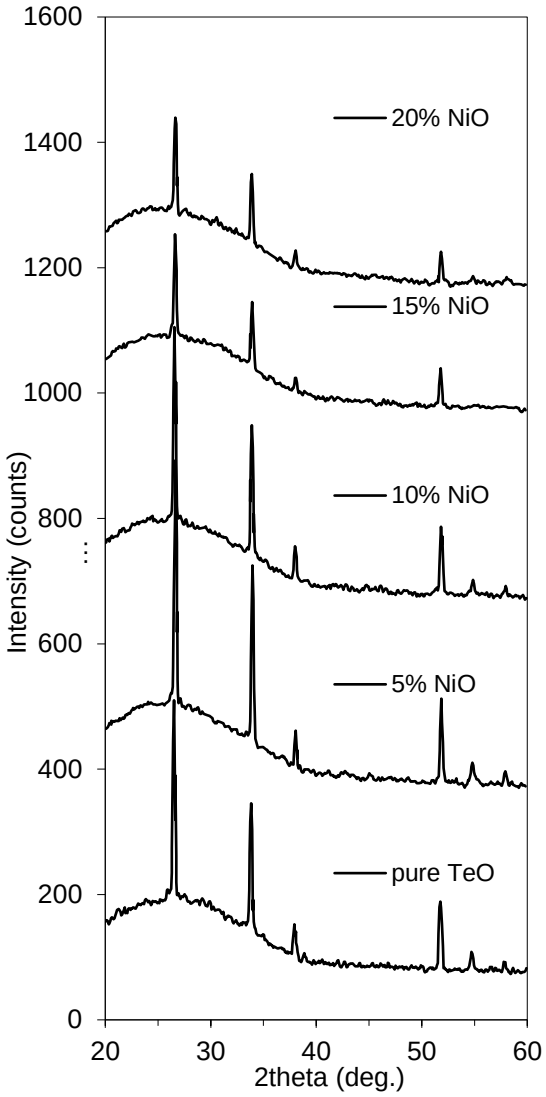

Fig. (2) X-ray diffraction patterns of pure TeO and doped with NiO films

It is well known that AFM is one of the most effective ways for the surface analysis due to its high resolution and powerful analysis. Figure (3) shows the surface morphology images of pure and doped TeO samples with different ratios of NiO. The images of the surface morphology of the pure and doped TeO films showed continuous and uniform surface homogeneity. The surface features of the films are comparable and the calculated surface roughness decreases from 7.73 to 5.63 nm with increasing NiO ratio to 10%, and when the doping ratio increases more than 10%, the roughness increases to 11.90 nm for doping ratio of 20%. It is clear that the doping lead to an effective decrease in the roughness of the TeO film especially at 10% NiO and after that increases to high values. Also, the AFM studies revealed that the grains have spherical shape and the average diameter particle size is about 115.09 nm for pure TeO film and there is a large change in the average diameter for doped film with 10% and 15% NiO, as the diameter decreases to 61.84 and 70.25 nm, respectively, and then return to increase to 119.43 nm for 20% doping

ratio. This means that there is a transformation to nanoparticles when the TeO films are doped with 10 and 15% NiO. Table (2) illustrates all parameters obtained from the surface morphology measurements.

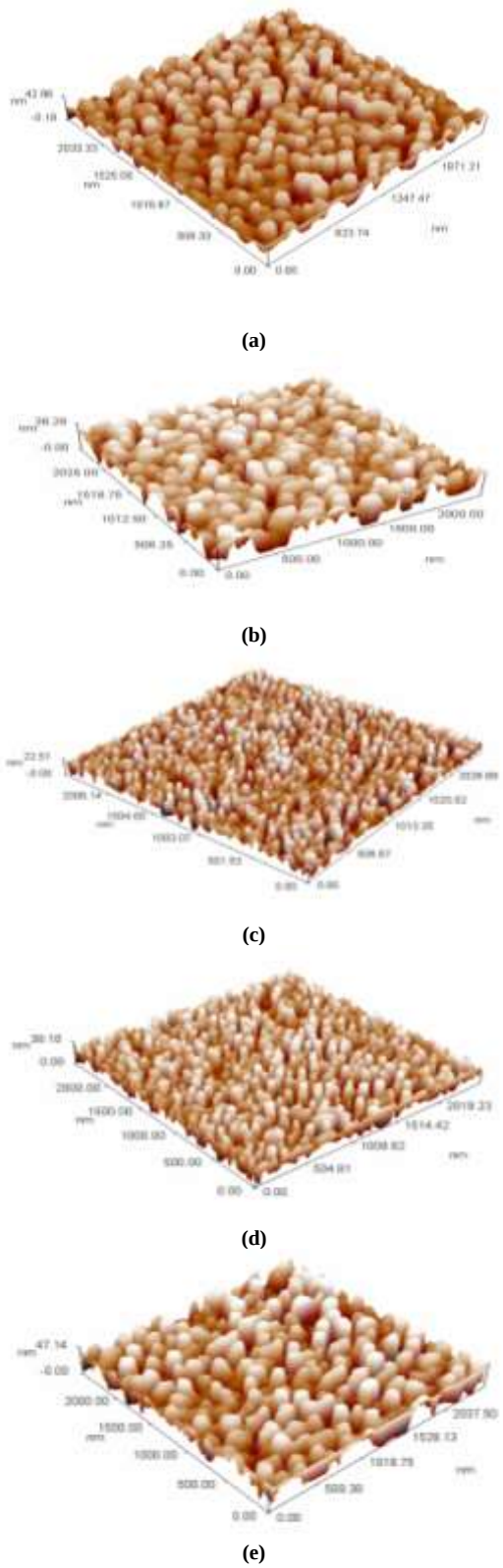

(a) **(b)** **(c)** **(d)** **(e)**

Fig. (3) 3D images of pure and doped TeO films (a) pure, (b) 5% NiO, (c) 10% NiO, (d) 15% NiO and (e) 20% NiO

4. Conclusion

This study revealed the effect of NiO additives on structural characteristics of TeO films deposited on glass substrates by pulsed laser deposition technique. The crystal structure studies indicate that the film crystallizes in tetragonal phase for TeO and monoclinic phase for NiO. The morphology of the samples exhibit uniform films those cover the substrate well, homogenous distribution, and the grain size decreases with increasing doping ratio and reaches minimum values at 10 and 15% NiO.

References

[1] A. Galdikas, A. Mironas and A. Šetkus, "Copper-doping level effect on sensitivity and selectivity of tin oxide thin-film gas sensor", Sensors & Actuators B, 26(1-3) (1995) 29-32.

[2] K.G. Godinho, A. Walsh and G.W. Watson, "Energetic and Electronic Structure Analysis of Intrinsic Defects in SnO_2", J. Phys. Chem., 113(1) (2009) 439-448.

[3] S.S. Pan et al., "Optical properties of nitrogen-doped SnO_2 films: Effect of the electronegativity on refractive index and band gap", J. Appl. Phys., 103(9) (2008).

[4] D. Scorticati et al., "Optical and electrical properties of SnO_2 thin films after ultra-short pulsed laser annealing", Proc. SPIE 8826, Laser Material Processing for Solar Energy Devices II, 88260I (2013) doi: 10.1117/12.2023635.

[5] O.A. Hamadi, "Characteristics of CdO-Si Heterostructure Produced by Plasma-Induced Bonding Technique", Proc. IMechE, Part L, J. Mater.: Design and Applications, 222(1) (2008) 65-71.

[6] Y. Shimizu and M. Egashira, "Basic aspects and challenges of semiconductor gas sensors", Mater. Res. Bull., 24(6) (1998) 18-24.

[7] K.S. Khashan and O.A. Hamadi, "Features of spot-matrix surface hardening of low-carbon steel using pulsed laser", Eng. Technol. J., 25(2) (2007).

[8] O.A. Hammadi and N.E. Naji, "Electrical and Spectral Characterization of CdS/Si Heterojunction Prepared by Plasma-Induced Bonding", Opt. Quant. Electron., 48(8) (2016) 375.

[9] S. Singh et al., "Synthesis and characterization of CuO–SnO_2 nanocomposite and its application as liquefied petroleum gas sensor", Mater. Sci. in Semicond. Process., 18 (February 2014) 88-96.

[10] O.A. Hammadi, "Characteristics of Heat-Annealed Silicon Homojunction Infrared Photodetector Fabricated by Plasma-Assisted Technique", Phot. Sen., 6(4) (2016) 345-350.

[11] F.J. Kadhim and A.A. Anber, "Fabrication of nanostructured silicon nitride thin film gas sensors by reactive direct current magnetron

sputtering", Proc. IMechE, Part N, J. Nanoeng. Nanosys., 231(4) (2018) 173-178.
[12] O.A. Hammadi, M.K. Khalaf, F.J. Kadhim, "Fabrication and Characterization of UV Photodetectors Based on Silicon Nitride Nanostructures Prepared by Magnetron Sputtering", Proc. IMechE, Part N, J. Nanoeng. Nanosys., 230(1) (2016) 32-36.
[13] R.G. Gordon, "Criteria for choosing transparent conductors", MRS Bulletin, 25(8) (2000) 52-57.
[14] O.A. Hamadi, "Characterization of SiC/Si Heterojunction Fabricated by Plasma-Induced Growth of Nanostructured Silicon Carbide Layer on Silicon Surface", Iraqi J. Appl. Phys., 12(2) (2016) 9-13.
[15] B. Zhang et al., "The FTIR studies on the structural and electrical properties of SnO_2:F films as a function of hydrofluoric acid concentration", Opt. Adv. Mater., 4(8) (2010) 1158-1162.
[16] O.A. Hamadi, B.A.M. Bader and A.K. Yousif, "Electrical Characteristics of Silicon p-n Junction Solar Cells Produced by Plasma-Assisted Matrix Etching Technique", Eng. Technol. J., 28 (2008).
[17] J.K. Srivastava, A. Gupta and A.A. Bhaskar, "Sensing Behavior Of CuO-Doped SnO_2 Thick Film Sensor For H_2S Detection", Int. J. Sci. Technol. Res., 3(5) (2014) 266-272.
[18] O.A. Hammadi, "Production of Nanopowders from Physical Vapor Deposited Films on Nonmetallic Substrates by Conjunctional Freezing-Assisted Ultrasonic Extraction Method", Proc. IMechE, Part N, J. Nanomater. Nanoeng. Nanosys., 232(4) (2018) 135-140.
[19] P.S. Pa, "Nanoscale Removal Fabrication for Touch Sensing Materials via Two Groups Mated Cylinder-Tool", Adv. Sci. Lett. 20(8) (2014) 95-98.
[20] J.C. Sohn et al., "H_2S Gas Sensing Properties of SnO_2:CuO Thin Film Sensors Prepared by E-beam Evaporation", Trans. Electr. Electron. Mater., 10(4) (2009) 135-139.
[21] R.K. Sonker et al., "Nanocatalyst (Pt, Ag and CuO) Doped SnO_2 Thin Film Based Sensors for Low Temperature Detection of NO_2 Gas", Adv. Sci. Lett., 20(7-9) (2014) 1374-1377.
[22] C. Wang et al., "Metal Oxide Gas Sensors: Sensitivity and Influencing Factors", Sensors, 10(3) (2010) 2088-2106.
[23] O.A. Hammadi, M.K. Khalaf, F.J. Kadhim, "Fabrication of UV Photodetector from NiO Nanoparticles Deposited on Silicon Substrate by CFUBDM Sputtering Technique", Opt. Quantum Electron., 47(12) (2015) 3805-3813.
[24] A. Chowdhuri et al., "H_2S gas sensing mechanism of SnO_2 films with ultrathin CuO dotted islands", J. Appl. Phys., 92(4) (2002) 2172.

Table (1) Structural parameters, such as 2θ values, inter-planar spacing, miller indices and grain size (G.S.) of pure TeO and doped with NiO films

Sample	2θ (deg.)	d_{hkl} Exp. (Å)	d_{hkl} Std. (Å)	*hkl*	G.S. (nm)	d_{NiO}	hkl_{NiO}	Phase
Pure TeO	26.560	3.3533	3.3503	110	9.9	-	-	Tetragonal
	33.880	2.6437	2.6440	101	10.3	-	-	Tetragonal
	37.980	2.3672	2.3670	200	10.5	-	-	Tetragonal
	51.800	1.7635	1.7640	211	10.4	-	-	Tetragonal
	54.720	1.6761	1.6750	220	9.9	-	-	Tetragonal
	57.820	1.5933	1.5933	002	11.3	-	-	Tetragonal
5% NiO	26.580	3.3508	3.3503	110	14.7	-	-	Tetragonal
	33.880	2.6437	2.6440	101	14.068	-	-	Tetragonal
	37.980	2.3672	2.3670	200	13.518	-	-	Tetragonal
	51.820	1.7628	1.7640	211	14.068	1.7690	112	Tetrag./monclinic
	54.760	1.6749	1.6750	220	12.987	-	-	Tetragonal
	57.860	1.5923	1.5933	002	15.344	1.5800	202	Tetrag./monclinic
10% NiO	26.560	3.3533	3.3503	110	9.3841	-	-	Tetragonal
	33.880	2.6437	2.6440	101	9.0942	-	-	Tetragonal
	37.960	2.3680	2.3670	200	9.9354	-	-	Tetragonal
	51.780	1.7640	1.7640	211	9.646	1.7690	112	Tetrag./monclinic
	54.740	1.6755	1.6750	220	9.3841	-	-	Tetragonal
	57.900	1.5913	1.5933	002	9.646	1.5800	202	Tetrag./monclinic
15% NiO	26.560	3.3533	3.3503	110	14.068	-	-	Tetragonal
	33.880	2.6437	2.6440	101	14.068	-	-	Tetragonal
	37.960	2.3684	2.3670	200	14.692	-	-	Tetragonal
	51.780	1.7641	1.7640	211	13.518	1.7690	112	Tetrag./monclinic
20% NiO	26.540	3.3558	3.3503	110	9.646	-	-	Tetragonal
	33.860	2.6452	2.6440	101	9.646	-	-	Tetragonal
	38.000	2.3660	2.3670	200	10.243	-	-	Tetragonal
	51.820	1.7628	1.7640	211	9.3841	1.7690	112	Tetrag./monclinic
	54.820	1.6732	1.6750	220	9.646	-	-	Tetragonal
	58.060	1.5873	1.5933	002	9.935	1.5800	202	Tetrag./monclinic

IRAQI JOURNAL OF APPLIED PHYSICS
Vol. 17, No. 3, July-September 2021, pp. 13-16

Effect of Using Organic Stabilizing Agent on Structural Characteristics of Cadmium Telluride Quantum Dots

Khaled B. Majjar
Lahcin M. Elshabbi
Elwan K. Elkhazri

Department of Electrical Engineering,
Faculty of Engineering,
University of Sfax,
Sfax, TUNISIA

In this work, cadmium telluride nanoparticles were synthesized by the aqueous solution method using organic stabilizing agent during preparation procedure. The optical, photoluminescence and structural characteristics of the synthesized quantum dots based on the prepared cadmium telluride nanoparticles were determined and studied. These quantum dots can be successfully used to improve the performance of photonics and optoelectronic devices, mainly photodetectors and solar cells.

Keywords: Cadmium telluride; Nanoparticles; Quantum dots; Aqueous solution

1. Introduction

Cadmium telluride is a stable crystalline II-VI compound that is combination of cadmium from column II and tellurium from column V of the periodic table. Semiconductor nanocrystals have been attracting wide interest due to their various potential applications such as in optoelectronic devices [1], photovoltaic devices [2], and biological fluorescence labeling [3]. Although biological fluorescence labeling with organic dye molecules has been the focus of intensive research for visualizing the cellular structure, studying the dynamic cellular processes and even tracking the path of single molecules in cells [4,5]. The intrinsic photophysical properties of organic fluorophores, which generally have broad absorption/emission profiles and low photobleaching thresholds, have limited their effectiveness in long-term imaging and multiplexing without complex instrumentation and processing [6].

Cadmium telluride crystal is transparent at the infrared wavelength (860nm), from close to its band gap energy which is approximately 1.44 eV at 300K to the wavelength greater than 20μm, which is already in the infrared region. It has been presented that if the size of the bulk cadmium telluride material shrinks to nanometer scale, normally 2 to 5 nm, the band gap energy of the material will increase, due to quantum confinement effect, meaning the fluorescence peak will shift towards the infrared region or even visible range. It has phase stable at 300K is zinc-blende structure or Wurtzite structure for various binary like II-VI compounds. The Wurtzite is an example of a hexagonal crystal system [7].

Quantum dots were developed recently as a new class of fluorescent probes have sparked intense excitement in the fields of biology and medicine, because they have shown higher sensitivity and better photostability and chemical stability than conventional fluorophore markers [8]. Many approaches, including organic synthesis [9] and aqueous synthesis [10-19] have been developed to prepare luminescent quantum dots. Also, several new techniques like, microwave irradiation [20], hydrothermal treatment [21] have been employed for rapid synthesis of high quality cadmium telluride nanocrystals in aqueous phase. For all the previous methods still the highly active and toxic NaHTe or H_2Te used as the Te source and selecting thiol stabilizers like glutathione or Mercaptopropionic (MPA) or Thioglycolic acid (TGA) or L-Cys.

In this work, the L-Cysteine acid was used to stabilize the cadmium telluride nanoparticles to produce quantum dots for photonics and optoelectronics applications.

2. Experimental Work

There are two common ways to synthesis QDs , the first method is top-down; by using the bulk semiconductor and thinned it to form QDs via the electron beam lithography or reactive-ion etching. The second method is bottom-up approach; which takes advantage of the chemistry and physics to artificially combine the atoms and molecules in a nanoparticles cluster. The bottom-up method will be used in this work.

The physical methods began with steps in which layers are grown in an atom by atom process as molecular beam epitaxy (MBE), physical vapor deposition (PVD) grows layer by condensing of solid from vapors by thermal evaporation or sputtering.

Some of the common synthesis processes for this method are: hydrothermal synthesis, sol-gel process, micro-emulsion process, hot solution decomposition process, and microwave synthesis process. In this

method, the parameters for a single solution or mixture of solution are controlling to precipitate, nucleuses are generated and further nanoparticles growth may be achieved.

These parameters are temperature, stabilizers, concentrations of precursors, ratios of anionic to cationic species and solvent, quantum dot of the desired size, shape and composition have been product. The preparation of cadmium telluride quantum dots takes place in several steps over two days period. The Materials that were used in this work, $NaBH_4$ sodium borohydride, tellurium powder, $CdCl_2.2.5H_2O$ cadmium chloride, Cysteine (L-cys), sodium hydroxide (NaOH), nitrogen gas.

The first step is the synthesis of NaHTe. The Te powder and sodium borohydride ($NaBH_4$) were combined in dry glass vial, in ratio Te:$NaBH_4$ =1:4. The vial shake to mix the powders and the 3-5ml of distilled water then added, the vial shake again on the magnetic stirrer. The mixture became dark grey and quickly lighted to grey in 3-4 seconds, a black layer formed at the surface of the mixture and some in the bottom while a bubbles observe in the solution ,which it color became purple. After that the vial was covered with plastic wrap have very small holes to let the hydrogen gas escape and put it in dark and cold place for 24 hours allowing the reaction as fully as possible to form NaHTe.

The second step was the preparation of the cadmium ion solution. The cadmium chloride dissolved in small amount of distilled water obeying the ratio Cd^{+2}:Te:L-cys = 3:1:6 .The $CdCl_2$ is white powder, but when dissolved in water the solution became clear solution. The buffer agent that used to capped the QDs added to the Cd^+ ions solution whose pH is 10.6 [the pH adjusted by several drops of NaOH (1M)]. The L-cys solution is a special amino acid. After mixing L-cys and Cd^+ ions, the solution is shown as a white precipitate immediately formed, then the solution transferred to a 3-neck flask with N_2 gas bubbled through the solution for 10 min.

Last step was the growth of quantum dots. The solution of Cd^+ ions was mixed by magnetic stirrer with heating by water bath to control the temperature of the process and using a condenser. The purple solution of NaHTe that previously prepared is added to the flask, the solution turned from white to orange and then lighted to golden-brownish within the first 15 min of growth.

The time period to growth the QDs was three hours then the sample was taken from the CdTe solution every 15 min.

3. Results and Discussion

The UV-visible absorption spectra were measured by Shimadzu UV-1800 spectrophotometer and used to calculate the optical energy gap. The photoluminescence (PL) spectra were recorded by Shimadzu spectrofluorophotometer and used to determine the optical energy gap using the following relation

$$E_g = 1240 / \lambda_{PL} \quad (1)$$

The absorption peaks for CdTe were shifted toward the longer wavelength as illustrated in table (1). It was found that the smaller nanoparticle size of CdTe nanoparticles have the lower energy band gap. So the sample 5 is the lowest nanoparticle size (10 nm), the peak wavelength of PL and the energy gaps for the samples also illustrated in table (1).

The XRD pattern is used for structure crystalline while the surface morphology study from SEM image to estimate the size of nanoparticles and give the shape of cluster nanoparticles. Heating process will promote CdTe QDs particle growth as well as crystallize the particles, with different heating time period starting from 15 to 180 minutes. The crystalline structure appear cubic when the samples were dried at room temperature for (111) plane as shown in Fig. (1), while the crystalline structure appears hexagonal when the samples (30 – 180 min) dried under vacuum at 400°C as shown in Fig. (2). The particles size calculated from sheerer formula for all samples were put in table (1). It can be estimated from SEM of the prepared samples that the CdTe QDs were formed as shown in Fig. (3).

Table (1) Effect of reaction time on absorption and PL peak wavelengths and energy band gap of the prepared QDs

Sample	Reaction Time (min)	Peak Absorption Wavelength (nm)	Peak PL Wavelength (nm)	Energy Band Gap (eV)
1	30	340	437	2.837
2	60	355	465	2.666
3	90	360	470	2.638
4	120	390	516	2.403
5	180	374-460	686	1.807

Table (2) illustrates the nanoparticle size obtained from the Scherrer's formula

$$D_1 = \frac{k\lambda}{\beta cos\theta} \quad (2)$$

and empirical fitting expression (Eq. 3) [23], and nanoparticles size estimated from the SEM image.

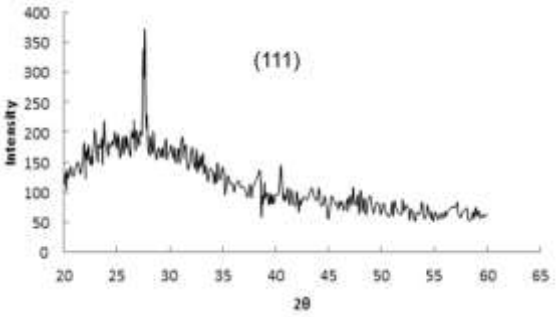

Fig. (1) XRD pattern of CdTe QDs prepared after drying at room temperature

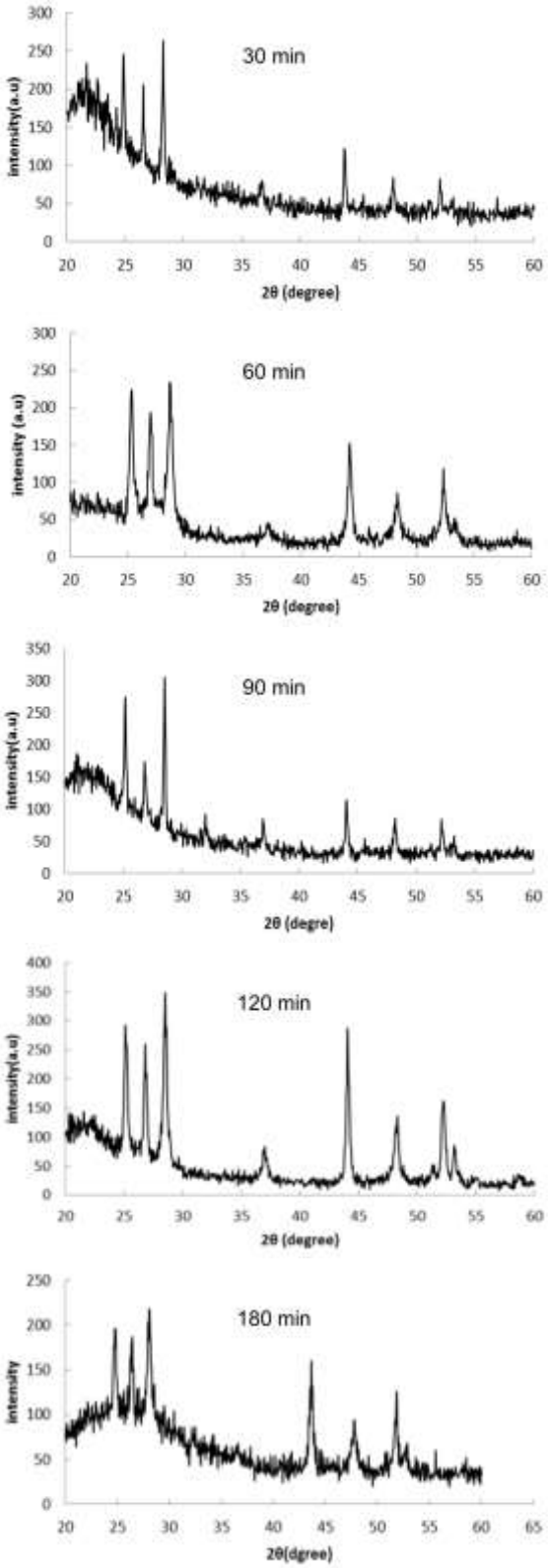

Fig. (2) XRD patterns of CdTe QDs after drying for 60 min at 400°C for (a) 30 min, (b) 60 min, (c) 90 min, (d) 120 min, and (e) 180 min

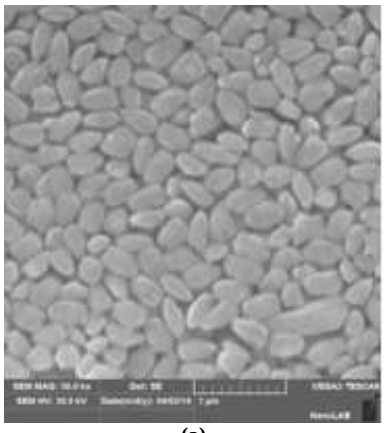

(a)

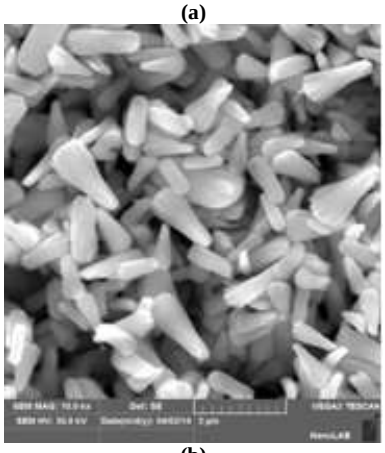

(b)

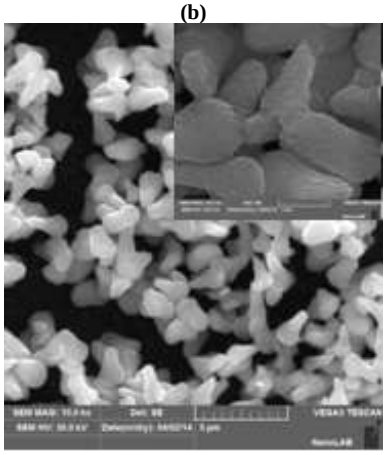

(c)

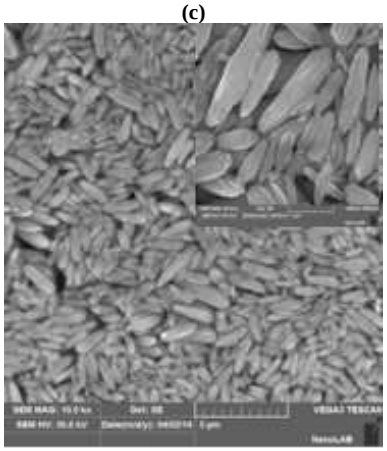

(d)

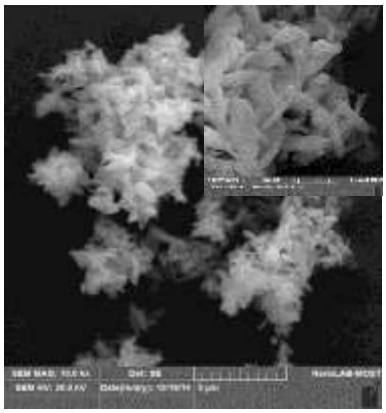

(e)

Fig. (3) SEM images of CdTe QDs for samples prepared after reaction time of (a) 30 min, (b) 60 min, (c) 90 min, (d) 120 min, and (e) 180 min

Table (2) Determination of nanoparticle size using Scherrer's formula and empirical fitting

Sample	D_1 (nm)	D_2 (nm)
1	26.47	12.3
2	20	9.7
3	16.42	8.9
4	11.556	4.9
5	10.975	3.8

4. Conclusions

In concluding remarks, cadmium telluride quantum dots with L-cysteine stabilizers were synthesized with stable pH of 10.69 that suits for different applications, as biological systems *in vitro* imaging and *in vivo* sensor. The effect of reaction time period is very controlling parameter that affect the size of cadmium telluride nanoparticles. The sample of 180 minutes had the lowest particle size (10nm), while the dimension of cadmium telluride rod was 1.8μm long and 0.2μm wide. The photoluminescence spectra get red shift and the intensity of luminescence increases till get stable size of cadmium telluride nanoparticles.

References

[1] D. Scorticati et al., "Optical and electrical properties of SnO_2 thin films after ultra-short pulsed laser annealing", Proc. SPIE 8826, Laser Material Processing for Solar Energy Devices II, 88260I (2013) doi: 10.1117/12.2023635.

[2] O.A. Hamadi, "Characteristics of CdO-Si Heterostructure Produced by Plasma-Induced Bonding Technique", Proc. IMechE, Part L, J. Mater.: Design and Applications, 222(1) (2008) 65-71.

[3] K.S. Khashan and O.A. Hamadi, "Features of spot-matrix surface hardening of low-carbon steel using pulsed laser", Eng. Technol. J., 25(2) (2007).

[4] O.A. Hammadi and N.E. Naji, "Electrical and Spectral Characterization of CdS/Si Heterojunction Prepared by Plasma-Induced Bonding", Opt. Quant. Electron., 48(8) (2016) 375.

[5] R.G. Gordon, "Criteria for choosing transparent conductors", MRS Bulletin, 25(8) (2000) 52-57.

[6] O.A. Hammadi, "Characteristics of Heat-Annealed Silicon Homojunction Infrared Photodetector Fabricated by Plasma-Assisted Technique", Phot. Sen., 6(4) (2016) 345-350.

[7] B. Zhang et al., "The FTIR studies on the structural and electrical properties of SnO_2:F films as a function of hydrofluoric acid concentration", Opt. Adv. Mater., 4(8) (2010) 1158-1162.

[8] O.A. Hammadi, M.K. Khalaf, F.J. Kadhim, "Fabrication and Characterization of UV Photodetectors Based on Silicon Nitride Nanostructures Prepared by Magnetron Sputtering", Proc. IMechE, Part N, J. Nanoeng. Nanosys., 230(1) (2016) 32-36.

[9] J.K. Srivastava, A. Gupta and A.A. Bhaskar, "Sensing Behavior Of CuO-Doped SnO_2 Thick Film Sensor For H_2S Detection", Int. J. Sci. Technol. Res., 3(5) (2014) 266-272.

[10] O.A. Hamadi, "Characterization of SiC/Si Heterojunction Fabricated by Plasma-Induced Growth of Nanostructured Silicon Carbide Layer on Silicon Surface", Iraqi J. Appl. Phys., 12(2) (2016) 9-13.

[11] O.A. Hamadi, B.A.M. Bader and A.K. Yousif, "Electrical Characteristics of Silicon p-n Junction Solar Cells Produced by Plasma-Assisted Matrix Etching Technique", Eng. Technol. J., 28 (2008).

[12] P.S. Pa, "Nanoscale Removal Fabrication for Touch Sensing Materials via Two Groups Mated Cylinder-Tool", Adv. Sci. Lett. 20(8) (2014) 95-98.

[13] O.A. Hammadi, "Production of Nanopowders from Physical Vapor Deposited Films on Nonmetallic Substrates by Conjunctional Freezing-Assisted Ultrasonic Extraction Method", Proc. IMechE, Part N, J. Nanomater. Nanoeng. Nanosys., 232(4) (2018) 135-140.

[14] J.C. Sohn et al., "H_2S Gas Sensing Properties of SnO_2:CuO Thin Film Sensors Prepared by E-beam Evaporation", Trans. Electr. Electron. Mater., 10(4) (2009) 135-139.

[15] R.K. Sonker et al., "Nanocatalyst (Pt, Ag and CuO) Doped SnO_2 Thin Film Based Sensors for Low Temperature Detection of NO_2 Gas", Adv. Sci. Lett., 20(7-9) (2014) 1374-1377.

$$\left[D_{\ 2} = \left(9.8127X10^{-7}\right)\lambda^3 - \left(1.7147X10^{-3}\right)\lambda^2 + \left(1.0064\right)\lambda - 194.84.....2\right] \quad (3)$$

IRAQI JOURNAL OF APPLIED PHYSICS
Vol. 17, No. 3, July-September 2021, pp. 17-20

Rafid J. Hameed
Maher H. Yaseen
Ahmed M. Jasim

Department of Physics, College of Education, University of Samarra, Samarra, IRAQ

Determination of Energy Band Outline of CoO:Au/Si Thin Film Solar Cells

In this work, thin film heterojunction solar cells were fabricated by the deposition of p-type gold-doped cobalt oxide layers on n-type silicon substrates using pulsed-laser deposition technique. The effects of the contact material on the photovoltaic characteristics of the fabricated solar cells. It was found that the conversion efficiency was higher than that of the p-CoO/n-Si thin film solar cells, which may attributed to the role of Au-doped CoO layer as a hole collector as well as a barrier for charge recombination.

Keywords: Solar cells, Band energy outline, CoO:Au thin films, Pulsed-laser deposition

1. Introduction

Magnetic metal/metal oxide particles have various fundamental and industrial applications. Cobalt is a special element that changes between two phase structures of hcp and fcc at a transition temperature of 450°C [1]. It is a ferromagnetic material, and due to such interesting properties, as good mechanical hardness, chemical stability and high electrical resistance, it has been used in many applications, including magnetic photocatalysts [2], high frequency magnets [3], information storage systems [4], magnetic bulk cores [5], microwave absorbers [6] and in biological applications, such as drug delivery [7], magnetic resonance imaging [8] and bio-sensors [9].

Cobalt oxide (CoO) is one of the most intensively investigated transition metal oxides. It is an antiferromagnetic oxide semiconductor with cubic structure. It can be a promising candidate for many applications such as solar thermal absorber [10], catalyst for O evolution [11], photoelectrolysis [12] and electrochromic device [13]. Cobalt oxide is also studied as the positive electrode in batteries [14]. Pure stoichiometric CoO crystals are perfect insulators [15]. Several efforts have been made to explain the insulating behavior of CoO. Appreciable conductivity can be achieved by creating Co vacancies or substituting lithium (Li) for cobalt (Co) at Co sites [15]. Hydrogen gas sensors based on electrostatically spray deposited CoO thin film was recently studied [16,17]. High efficient electrical devices can be fabricated by doping cobalt oxide with gold.

Pulsed-laser deposition (PLD) is one of the most important and powerful techniques for thin film deposition of complex materials. It consists of three major parts, laser source, vacuum system and deposition chamber [18]. Electrical properties of pure CoO and CoO:Au thin films prepared by PLD has been intensively [19].

Solar cell or photovoltaic cell is an electrical device that converts the energy of light directly into electricity by the photovoltaic effect which is a physical and chemical phenomenon. Solar cells are described as being photovoltaic irrespective of whether the source is sunlight or an artificial light [20]. They are used as a photodetector, detecting light or measuring light intensity [21]. Recent studies have been shown that CoO thin films can be used successfully as solar cell.

A photovoltaic (PV) cell may be represented by the equivalent circuit model 2420 [22]. The more important characteristic of PV are conversion efficiency (η) and fill-factor that defined as [22]:

$$\eta = \frac{maximum\ output\ power\ (P_m)}{input\ power\ (P_{in})} \quad (1)$$

and the fill-factor (FF) is define as:

$$FF = \frac{I_m V_m}{I_{SC} V_{OC}} \quad (2)$$

where P_{in} is the power input to the cell, V_{oc} open circuit voltage, I_{sc} is the short circuit current, and I_m and V_m are the maximum cell current and voltage respectively at the maximum power point, $P_m = I_m . V_m$. Figure (1) illustrates the typical (I-V) characteristic of a Si PV cell, showing I_m and V_m at the maximum power point. Solar cell behavior can conveniently be examined through four main parameters as shown in Fig. (1).

2. Experimental Part

The PLD experiment was carried out inside a chamber initially evacuated to 10^{-3} Torr [23]. The main experimental parameters of laser source are 532 nm wavelength, 1000 mJ pulse energy, 10 ns pulse width, 5 Hz repetition frequency and 100 number of shots. The substrate (Si) is placed in front of the target (CoO with different doping ratio of Au) with its surface parallel to that of the target. Sufficient gap is kept between the target and the substrate so that the substrate holder does not obstruct the incident laser beam. The temperature of Si substrate was 100°C.

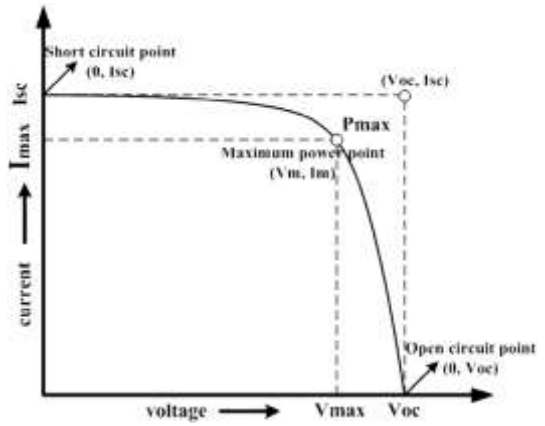

Fig. (1) Forward bias I-V characteristic of typical Si PV cell [11]

Different Au doping ratios (0,1, 2, and 4 wt. %) of CoO were used to prepare the CoO:Au/Si structure. The thicknesses of films were measured to be about 400 nm for all samples while the area (A) was about 1 cm^2. A typical scheme of the fabricated device is shown in Figure (2).

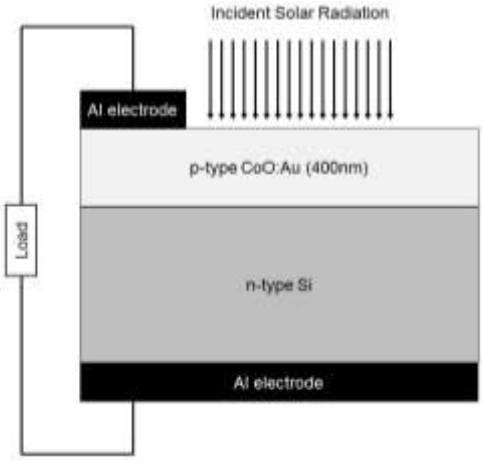

Fig. (2) Schematic diagram of the CoO:Au/Si solar cell fabricated in this work

A digital muitimeter victor VC97 was used to measure the current flow in a detector, manufactured from the prepared structure in dark condition. Voltage was applied from a KIETHLEY power supply at arrange of 0-5V in forward and reverse biasing conditions. This characterization was used to determine the conversion efficiency (η) and fill-factor (FF), where the power input (P_{in}) to the cell of 50 mW.

3. Result and Discussion

The morphology of thin films of pure and Au-doped CoO films deposited on Si substrates by PLD at 100°C temperature was examined using SEM. Figure (3) shows that all films are homogeneously distributed, very smooth and the crystallites are very fine.

Table (1) shows the effect of doping ratio on conductivity (σ) and energy band gap (E_g) of CoO. From the result, one may conclude that adding a small amount of Au in CoO material enhances the conductivity of the CoO because the conductivity of Au is higher than CoO, moreover the energy gap of CoO will be decrease.

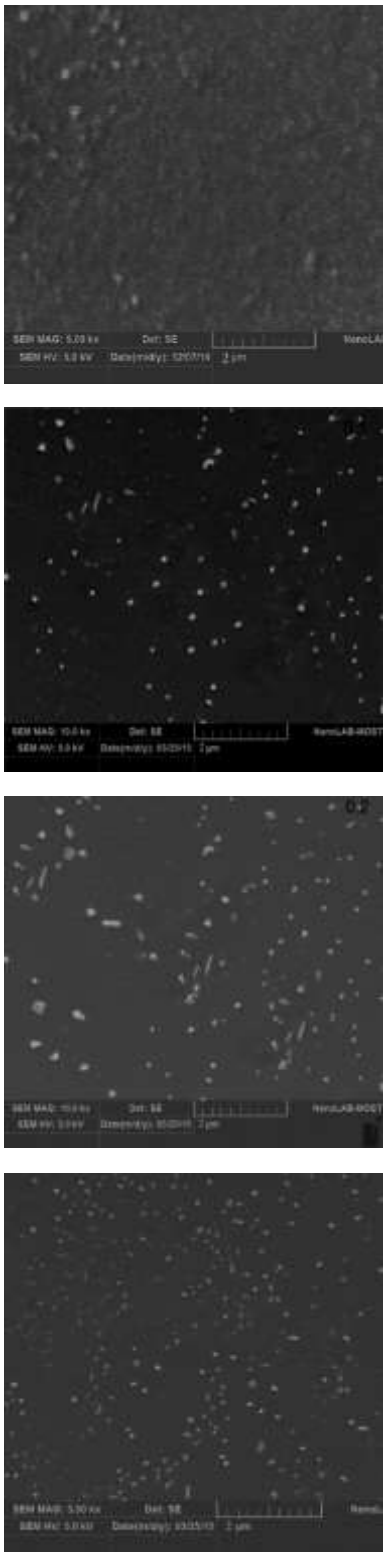

Fig. (3) SEM images for (a) pure CoO and (b and c) Au-doped CoO thin films at room temperature

Table (1) Effect of doping with gold on conductivity and energy band gap of CoO films

Sample	σ (Ω. cm^{-1})	E_g (eV)
Pure	4.17x10^{-6}	3.60
0.1	3.35x10^{-4}	3.50
0.2	2.34x10^{-3}	3.45
0.4	8.46x10^{-2}	3.4

Heterojunctions between p-type CoO with different doping ratios and n-type Si substrate is formed. The dark I-V curve in the forward and reverse bias for cell constructed with CoO:Au/Si as shown in figures (4), (5), (6) and (7). The doping ratio (wt.%), short-circuit current (I_{sc}), the open-circuit voltage (V_{oc}), maximum power points (V_m and I_m), fill-factor (FF) and conversion efficiency (η) were listed in Table (2). It is concluded from this table that the highest value of conversion efficiency was obtained at 0.4 wt.% doping ratio. The device had an open-circuit voltage of 0.21, short-circuit current of of 182 mA, and maximum power points (V_m and I_m) of 0.08 and 115, respectively. The conversation efficiency (η) derived from Fig. (7) is 18.4%.

The solar cell made without Au doping give lower values of conversion efficiency (η) (~0.84%) at the same illumination intensity. From the results presented above, it is clearly seen that the CoO:Au layer on Si substrate acts as a hole collector, so this kind of solar cells can be improved for a future work to give much higher efficiency. To illustrate the relationship between the conversion efficiency with doping ratio, figure (8) shows the gradual increase in conversion efficiency at 0.1 wt.% doping ratio. This increase becomes higher to reach 16.38%. Finally, a slight increase in the conversion efficiency is observed to reach a maximum value of 0.4%. The effect of doping on open-circuit (V_{oc}) and short-circuit current (I_{sc}) is shown in Fig. (9), where both increase with increasing the doping ratio.

Table (2) The cell parameters for CoO:Au/Si solar cells of 1 cm^2 area and incident power (P_{in}) of 50 mW

N	I_{sc} (mA)	V_{oc} (V)	I_m (mA)	V_m (V)	Fill factor (F.F)	Efficiency (η%)
Pure	10	0.16	7	0.06	0.262	0.84
0.1	30	0.14	14	0.08	0.266	2.24
0.2	180	0.178	105	0.078	0.255	16.38
0.4	185	0.21	115	0.8	0.252	18.4

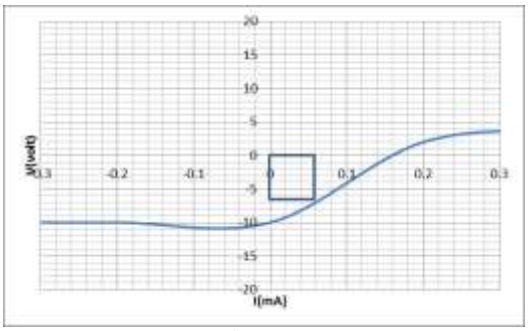

Fig. (4) I-V curve for pure CoO/Si solar cell

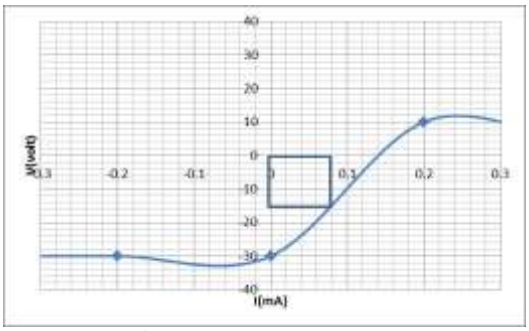

Fig. (5) I-V curve for CoO:Au/Si solar cell with Au doping ratio of 0.1 wt.%

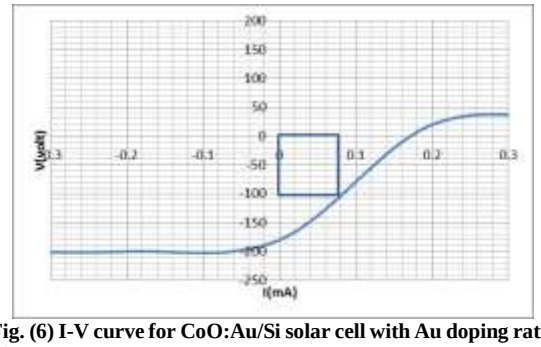

Fig. (6) I-V curve for CoO:Au/Si solar cell with Au doping ratio of 0.2 wt.%

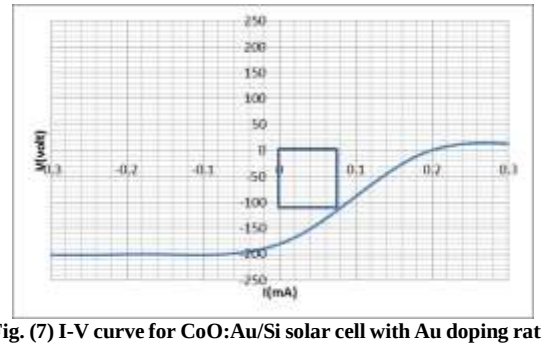

Fig. (7) I-V curve for CoO:Au/Si solar cell with Au doping ratio of 0.4 wt.%

4. Conclusion

According to results presented in this work, it can be concluded that the CoO:Au/Si thin film structures can be used as heterojunction solar cells, where the highest value of conversion efficiency can be obtained at doping ratio of 0.4 wt.%. The CoO:Au layer acts as a p-type layer on n-type Si substrate, so it can be used as a hole collector to improve the performance of the solar cells based on these structures.

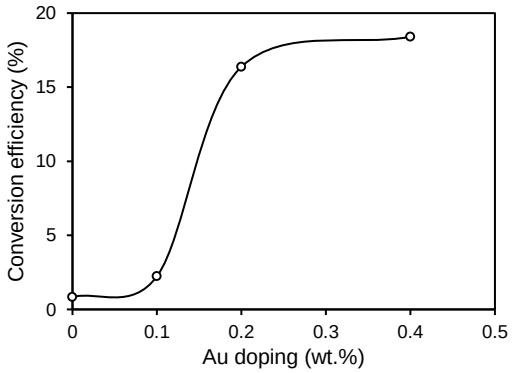

Fig. (8) Conversion efficiency (η) vs. Au doping ratio for the CoO:Au/Si solar cells fabricated in this work

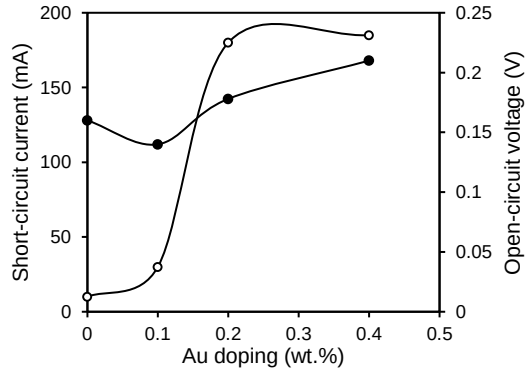

Fig. (9) Variation of V_{oc} (black circles) and I_{sc} (white circles) with Au doping ratio of CoO layer

References

[1] M. Jiang, K. Oikawa and T Ikeshoji, "Molecular-dynamic simulations of martensitic transformation of cobalt", Metall. Mater. Trans., A36 (2005) 2307-2314.

[2] O.A. Hammadi, "Photovoltaic Properties of Thermally-Grown Selenium-Doped Silicon Photodiodes for Infrared Detection Applications", Phot. Sen., 5(2) (2015) 152-158.

[3] S. Nomura and T. Isobe, "Design Study on High-Frequency Magnets for Magnetic Hyperthermia Applications", IEEE Trans. on Appl. Supercond., 28(3) (2018) 1-7.

[4] A.A.K. Hadi and O.A. Hamadi, "Optoelectronic Characteristics of As-doped Si Photodetectors Produced by LID Technique", Iraqi J. Appl. Phys. Lett., 1(2) (2008) 23-26.

[5] M. Zhang et al., "Soft magnetic properties of bulk FeCoMoPCBSi glassy core prepared by copper mold casting", J. Appl. Phys., 111(7) (2012) 07A312.

[6] O.A. Hamadi, "Characterization of SiC/Si Heterojunction Fabricated by Plasma-Induced Growth of Nanostructured Silicon Carbide Layer on Silicon Surface", Iraqi J. Appl. Phys., 12(2) (2016) 9-13.

[7] S. Iravani and R.S. Varma, "Sustainable synthesis of cobalt and cobalt oxide nanoparticles and their catalytic and biomedical applications", Green Chem., 22(9) (2020) 2643-2661.

[8] O.A. Hamadi, B.A.M. Bader and A.K. Yousif, "Electrical Characteristics of Silicon p-n Junction Solar Cells Produced by Plasma-Assisted Matrix Etching Technique", Eng. Technol. J., 28 (2008).

[9] B.K. Pandey, A.K. Shahi and R. Gopal, "Magnetic colloid by PLA: Optical, magnetic and thermal transport properties", Appl. Surf. Sci., 347 (2015) 461-470.

[10] J.G. Cook and F.P. Koffyberg, "solar thermal absorber employing oxide of Ni and CO", Solar Energy Mater., 10 (1984) 55.

[11] J.C.N. Botejue and A.C.C. Tseung, "Oxgen evolution on nickel oxide electrodes", J. Electrochem. Soc., 132 (12) (1985) 2957.

[12] F.P. Koffyberg and F.A. Benko, "p-type NiO as a photoelectrolysis cathode", J. Electrochem. Soc., 128(11) (1981) 2476.

[13] C.M. Lampert, Solar Energy Materials and Solor Cells, (11) (1984) 27.

[14] C.A. Vincent et al., **"Modern Batteries"**, 1st ed., Edward Arnold (London, 1987).

[15] A.J. Bosman and C. Crevecoeur, "Mechanism of the electrical conduction in Li-doped NiO", Phys. Rev. Lett., 144 (1966) 763.

[16] R.K. Jamal et al., "Preparation and of nickel oxide thin film by electrostatic spray technique", Iraqi J. Sci., 57(1C) (2016) 618-623.

[17] R.K. Jamal and I.N. Tabban, "Electrical properties of pure NiO and NiO:Au thin film prepared by using pulse laser deposition", Iraqi J. Phys., 14(29) (2016) 37-43.

[18] M. Tom, An experimental study on the preparation of gold nanoparticles and their properties, PhD thesis, University of Leuven (2006).

[19] R.K. Jamal, Q.G. Al-zaidi and I.N. Taaban, "Hydrogen gas sensor based on electrostatically spray deposition nickel oxide thin film structures", Phot. Sen., 5(3) (2015) 235-240.

[20] S.H. Faisal and M.A. Hameed, "Heterojunction Solar Cell Based on Highly-Pure Nanopowders Prepared by DC Reactive Magnetron Sputtering", Iraqi J. Appl. Phys., 16(3) (2020) 27-32.

[21] O.A. Hammadi, M.K. Khalaf and F.J. Kadhim, "Fabrication of UV Photodetector from Nickel Oxide Nanoparticles Deposited on Silicon Substrate by Closed-Field Unbalanced Dual Magnetron Sputtering Techniques", Opt. Quantum Electron., 47(12) (2015) 3805-3813.

[22] Measuring Photovoltaic cell I-V characteristics with model 2420 source meter instrument, ApplicationNote Series, from KEITHLEY, company (number 1953).

[23] A.V. Rode, E.G. Gamaly and B. Luther-Davies, **"Ultrafast Laser Ablation and Film Deposition"**, Marcel Dekker, Inc. (NY, 2007).

IRAQI JOURNAL OF APPLIED PHYSICS
Vol. 17, No. 3, July-September 2021, pp. 21-26

Neerat S. Sharma
Ramaswami Kumar
Arvand Raj Krishna

Department of Chemistry, Faculty of Science, University of Mishra, Mishra, INDIA

Resistance-Time Characteristics of MEH-PPV/Si Device for Gas Sensing Applications

In this work, MEH-PPV/Si and MEH-PPV/PS at different current densities have been synthesized for NO_2 gas sensor. The sensitivity and speed response at different operating temperatures (RT, 100°C, 200°C). The study showed that the maximum sensitivity to NO_2 gas for MEH-PPV/Si sensor is 16% at RT, and the maximum sensitivity to NO_2 gas is 74% at 200°C. Results show that MEH-PPV/PS has better sensitivity toward nitrogen dioxide gas compared to MEH-PPV/Si.

***Keywords*:** Organic heterojunction; MEH-PPV gas sensor; Conductive polymers

1. Introduction

Conducting polymers, such as (poly[2-methoxy-5-(2-ethylhexyloxy)-1,4phenylenevinylene)] (MEH-PPV), have been used as the active layers of gas sensors. In comparison with most of the commercially available sensors, the sensors made of conducting polymers have many improved characteristics [1]. They have high sensitivities and short response time; especially, these features are ensured at room temperature. Conducting polymers are easy to be synthesized through chemical or electrochemical processes, and their molecular chain structure can be modified conveniently by copolymerization or structural derivations. Furthermore, conducting polymers have good mechanical properties, which allow a facile fabrication of sensors. As a result, more and more attentions have been paid to the sensors fabricated from conducting polymers, and a lot of related articles were published. There are several reviews emphasize different aspects of gas sensors and some others discussed sensing [2,3].

Alternatively to PS surface modification by small functional groups, polymer-PS heterojunction presents attractive functional material for gas sensing. Such heterojunction structures can be prepared by various techniques, including direct polymer infiltration from solution, polymer grafting, polymerization from monomers, etc. [4], in many cases major, polymers within a porous structure are used for vapor sensing applications. Thechallenge of polymer infiltration is the deep and uniform pores filling so that polymer covers the pores walls as a thin film without pore clogging. The pores should be hollow and accessible for the interaction with analyte molecules from the outer atmosphere [5]. NO_2 is one of the main toxic components emitted from vehicular exhaust and also a main component of emissions from indoor appliances. In addition, it transforms in the air to form gaseous nitric acid and toxic organic nitrates, hence contributing to the production of acid rain. Therefore a selective and accurate NO_2 sensor is of extreme importance for continuous monitoring of emission processes [6].

Sensitivity is the ability of a device to detect a variation in a physical and/or chemical property of the sensing material under gas exposure. In order to improve the sensitivity, it will be of great interest to work with the most appropriate sensing material in every case and to obtain its optimum detecting temperature [7]. Taking into account that sensing reactions take place mainly at the sensor's surface layer, the control of semiconductor composition, morphology and microstructure are required for enhancing the sensitivity of the sensor. Working with nanostructure materials will give a higher surface.

Also sensitivity is defined by the resistance change when the sensor is exposed to a certain concentration of gas. The sensitivity can be calculated as given in [8]:

$$S = \left|\frac{R_g - R_a}{R_a}\right| \times 100\% \qquad (1)$$

where S is the sensitivity, R_a isthe electrical resistance of the film in the air and R_g is electrical resistance of the film in the presence of gas. And also it can be calculated by using an equation [9]:

$$S = \left|\frac{R_g - R_a}{R_a c}\right| \times 100\% \qquad (2)$$

where c is the gas concentration. As well as it can be calculated by conductivity using an equation [10]:

$$S = \frac{\sigma_g}{\sigma_a} \qquad (3)$$

where σ_a is the conductivity of the film in the air and σ_g is the conductivity of the film in the presence of gas

The response time of a gas sensor is defined as the time required for the sensor to reach 90% of maximum/minimum value of conductance upon introduction of the reducing/oxidizing gas. Similarly, the recovery time is defined as the time required recovering to within 10% of the original baseline when the flow of reducing or gas is removed. The

response time and recovery time can be calculated as follows [11]:

Response time = $|t_{gas(on)} - t_{gas(off)}|$ x0.9 (4)

Recovery time = $|t_{gas(off)} - t_{gas(recovery)}|$ x0.9 (5)

The goals of this paper is fabrication MEH-PPV/Si and MEH-PPV/PS gas sensor devices by spin coating technique and study structure, morphology of the organic- polymer composite, and sensitivity to NO_2 gas.

2. Experimental work

In this work, the details of various experimental procedures and measurements used for synthesis of gas sensing samples are described.

The porous silicon (PS) structure is formed by photoelectrochemical etching **(PECE)** technique of silicon wafers porous silicon on n-type silicon, illumination method is the most popular way to generate holes required in the electrochemical etching process, the photo energy absorption by the atoms depends on the intensity of the illumination source, the distance from the source and the electrolyte environment. Therefore, only the surface layer under the illumination generates electron hole pairs. But the etching rate gradually decreases with time as it is very difficult to reach the illumination into the deep area of the pores. An electrolyte including hydrofluoric acid (HF) and surfactants (mainly ethanol). Because the cleaned, polished Si wafer surface is hydrophobic, porous silicon layer were produced using monocrystalline silicon wafers n-type, with resistivity of 10 Ω.cm [12]. The silicon wafers used in this work with (111) orientation the actual photo-energy absorbing by Si atoms is very sensitive to the illumination-source intensity. The effects of current density were investigated at: 20, 40, and 50 mA/cm^2 at 10 min etching time.

The samples were prepared by using spin coating technique MEH-PPV films were prepared at the concentration of about 0.01:2 mg/ml of solvent in which the polymer MEH-PPV Chloroform were used a solvent; the solutions were spin coated on , silicon MEH-PPV/Si and porous silicon MEH-PPV/PS (111) substrates.

The (poly[2-methoxy-5-(2-ethylhexyloxy)-1,4 phenylenevinylene)] MEH-PPV $(C_{18}H_{28}O_2)_n$ (average M.W. 40,000-70,000, Sigma-Aldrich) conducting polymer, MEH-PPV was synthesized by Wudl and Srdanov in 1993 [13]. The MEH-PPV was used to prepare the blends films. Stock solutions of MEH-PPV (10 mg/mL) and stirred prior casting onto n-Si and n-PS substrates.

Spin coating is a common method to produce uniform thin films of organic materials on flat substrates. This technique also can be used on fabricating of the colloidal sphere arrays by spin-coating at around 1000 rpm at1.5 minute period time, the colloidal dispersions on substrates. Evaporation of the solvent in the dispersion can be accelerated by spin-coating so when the liquid becomes almost as thick as the diameter of the spheres, a strong immersion capillary attraction arises between the particles and assists the self-organization of the particles.

In this process, excessive amount of suspension is placed on the wafer Si and PS then rotated at a high speed around the axis perpendicular to the substrate plane in order to spread the fluid by centrifugal force. Due to the centripetal acceleration, most of the suspension is flung off the edge of the substrate, leaving a thin film of the particles after evaporation of the liquid on the wafer surface [14,15]. The process is divided into four distinct stages so that the physics of the process can be well modeled. The four stages are deposition, spin-up, spin-off and evaporation of solvent [16].

For the fabrication, n-type single crystal silicon (111) and MEH-PPV was used. For formation of ohmic contact, high purity (99.999%) Al was thermally evaporated in vacuum coating system. The film of (MEH-PPV) was deposited by spin coating on Si. Al metal contacts were formed on MEH-PPV organic layer by vacuum thermal evaporation.

The anode was composed of silicon wafer, while the cathode was composed of platinum or any HF–resistant and conducting material. The cell body was composed of a highly acid–resistant polymer, such as Teflon. Silicon wafer surfaces that served as anodes in contact with HF solution, including the cleaved edges. The advantage of this equipment is its simplicity [17]. PS samples (n–type) were prepared at current density of (20, 40, 50) mA/cm^{2}andetching time (10min). In addition, organic conducting polymer MEH-PPV was deposited on the PS surface to obtain high conductivity.

The gas sensing measurements for MEH-PPV which are deposited on the Si and PS substrates were achieved to fabricate gas sensors.

Vacuum evaporation technique utilizing Edward coating unit model 306 under vacuum of 10^{-5} mbar. PC-interfaced digital multimeter of type UNI-T UT81B and Laptop PC are used to register the variation of the sensor resistance when it was exposed to air-NO_2 gas mixing ratio.

3. Results and Discussion

The sensing properties of MEH-PPV deposited on Si and porous silicon substrates are realized as a function of operating temperature and time to find the temperature dependence of the sensitivity for NO_2.

The sensing mechanism for MEH-PPV deposited on the n-type silicon, for gas sensing using NO_2 with concentration of 25 ppm at different operation temperatures beginning from room temperature (30°C) up to 200°C. Figure (1) shows the difference of resistance as a function of time with on/off gas amount. Figures show decreasing in the resistance value when the devices were exposed to NO_2 gas, (Gas ON), then the resistance value increases with the closure of the gas (Gas OFF). The reason for this

behavior can be attributed to the following: NO_2 gas undergoes an ionic reaction with the surface adsorption oxygen, where the electron on the oxygen, is extracted from the semiconductor so, the holes will increase in this p-type organic material [21] and causes the conductivity of the MEH-PPV materials to increase, thus causing the resistance to decrease [22].

The operating temperature is defined as the temperature at which the resistance of the sensor reaches a constant value. Changing of resistance is just only influenced by the presence of amount of some gases of interest [23]. The sensitivity factor (S%) at various operating temperatures is calculated using equation (2). Results show that the sensitivity equals to 8.6% for NO_2 gas at 100°C [see table 1].

Table (1) Response time, recovery time and sensitivity of MEH-PPV/Si device as a function of operating temperature

Temperature	Response time (s)	Recovery time (s)	Sensitivity (%)
RT	35	23	16.6
100°C	21	80	8.6
200°C	0	0	0

From Fig. (1), the response and recovery times have been determined from eqs (4) and (5). Response time is 21s and recovery time of 80s at 100°C operating temperature. The sensing properties of MEH-PPV deposited on the PS (n-type) at constant time of 10 min and different etching currents of 20, 40, 50 mA were investigated as a function of operating temperature to find the temperature dependence of the sensitivity for NO_2 gas. It was found that there is sensitivity for the samples at the current densities 20, 40, 50 mA at different operation temperature beginning from room temperature (30°C) up to 200°C with step of 50°C. Figure (2) shows the variation of resistance as a function of time with on/off gas valve. Changing in conductivity essentially is due to the enhancement of the conductivity related to the presence of conducting polymer inside the porous template. The conductivity enhancement after polymer deposition indicated that the possibility for complete oxidation of PS layer was excluded during polymer deposition.

The sensitivity factor (S%) at various operating temperatures (RT, 100°C, 150°C, 200°C) is calculated using equation (2). Figure (3) shows the sensitivity as a function of operating temperature for MEH-PPV, which are deposited on the PS (n-type) substrates. Increasing the operating temperature leads to an improvement of the device sensitivity which is attributed to increase in the rate of surface reaction of the target gas.

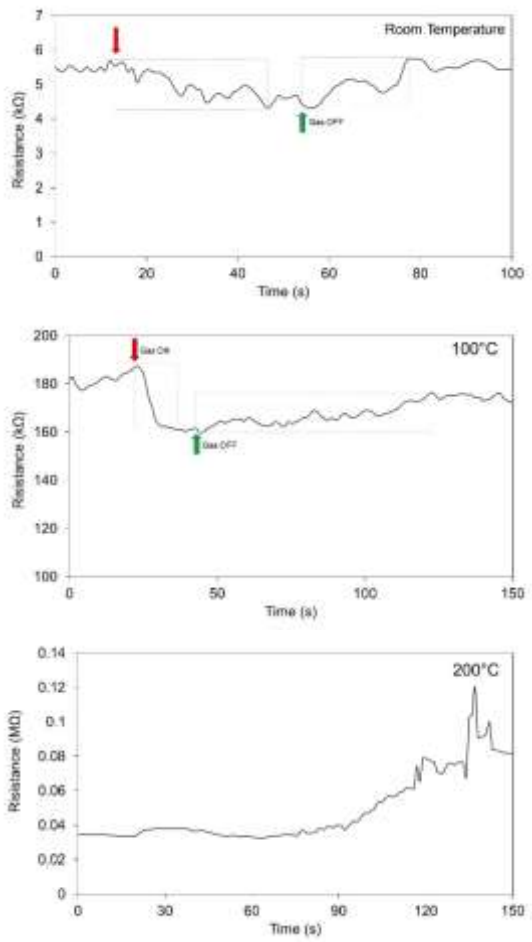

Fig. (1) The variation of resistance with time for MEH-PPV/Si device as NO_2 gas sensor

The sensitivity of MEH-PPV/PS (n-type) from RT to 200°C. The reason for this may be that of limited diffusion to polymer chains remotely located from the surface, since enough polymer mass is distributed inside the porous structure. Presumably this interesting effect can be associated with weaker binding of molecules to polymer chains distributed less densely in the porous medium than in the solid film [24], or may be due to the contrary to the porosity, total number of high/low porous layers, etching at lower temperatures, or higher viscosities to improve the interface sharpness between layers with high and low porosities, using different types of emissive polymers (small molecules) and functionalizing the PS surface. Thus, the gas sensitivity decreases [25]. While, at the current density 40 mA to MEH-PPV/PS (n-type) the sensitivity is slowly increased as the temperature increased from RT to 200°C.

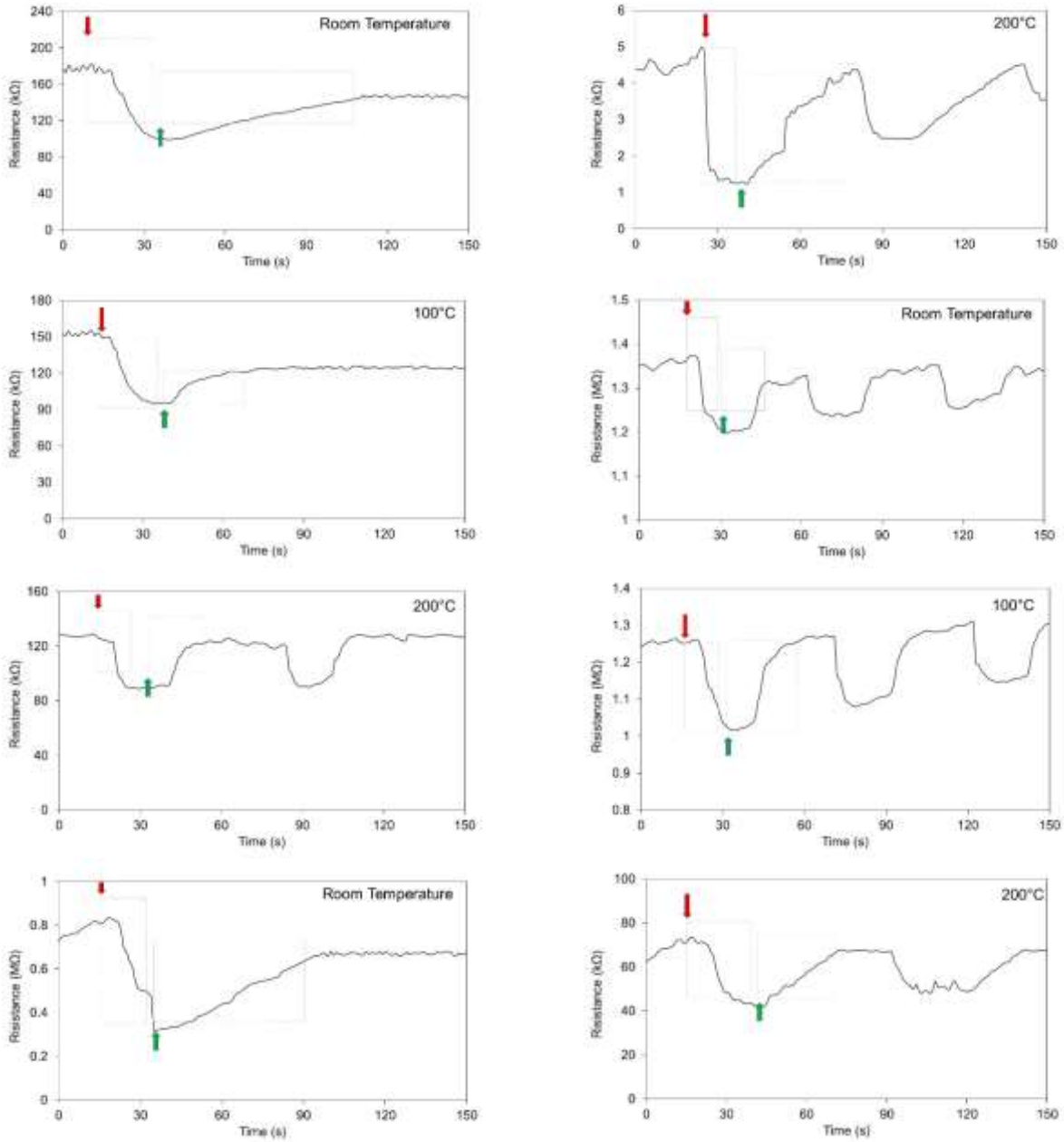

Fig. (2) The variation of resistance with time for MEH-PPV/PS device which different current densities (20, 40, 50 mA/cm^2) as NO_2 gas sensing

The increase of sensitivity may be due to the large interfacial area, a quasi-monomolecular layer of polymer adsorbed on pore walls, negligible pore clogging, and efficient diffusion of gas vapor inside the nanoporous structure due to capillary forces [26]. in addition to the heating process allows a rearrangement of the polymer chains and the directivity within the polymer matrix, leading to an increase of interfaces between MEH-PPV and PS for optimal efficiency, and the optimum surface roughness, porosity, large surface area [27].The sensitivity for MEH-PPV/n-type PS increased as temperature increasing .The sensitivity is reduced gradually with increasing of temperature for etching current of 20 and 50 mA. [see table 2].

Table (2) Response time, recovery time and sensitivity% of MEH-PPV/PS (p,n-type) device with different current densities

Current Density (mA/cm^2)	Response time (s)		
	RT	100°C	200°C
20	25	3	13
40	15	16	13
50	28	26	24
	Recovery time (s)		
20	68	30	21
40	55	43	38
50	28	38	18
	Sensitivity (%)		
20	43.5	37.5	29.6
40	63.4	67.6	74.8
50	36.7	18	3.3

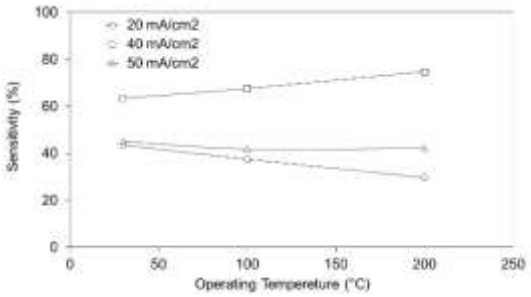

Fig. (3) The variation of sensitivity with operating temperatures for MEH-PPV/PS (n-type) for NO_2 gas

Figures (4a,b) show the response time and the recovery time as a function of operating temperature at different etching currents densities 20, 40, 50 mA/cm^2 for the MEH-PPV deposited on PS (n-type) wafer for NO_2 gas. The response speed is studied at the temperature at which the sensor exhibited a maximum sensitivity. Figures (4a,b) show that at etching current of 40 mA the sample exhibits a fast response speed of 13s to MEH-PPV/PS (n-type) at 200°C, recovery time of 38s at 200 °C MEH-PPV/PS (n-type). The quick response sensor for NO_2 gas may be due to faster oxidation of gas [28].

4. Conclusions

In concluding remarks, the MEH-PPV conducting polymer is deposited on crystalline silicon and porous silicon substrates by spin coating technique. The obtained results revealed that MEH-PPV has sensing properties for toxic gases such as NO_2 and the sensor device has good sensitivity for thin films deposited on porous silicon substrate as compared to those deposited on crystalline silicon substrate.

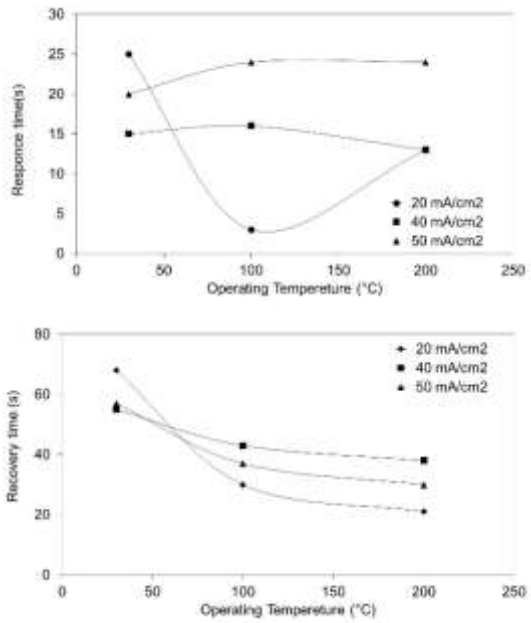

Fig. (4) The variation of response time (a) and recovery time (b) with operating temperature of the MEH-PPV deposited on PS (n-type)

References

[1] C. Nylabder, M. Armgrath and I. Lundstrom, "An ammonia detector based on a conducting polymer", Proc. Int. Meeting on Chem. Sensors, Fukuoka, Japan, 1983, 203-207.

[2] A. Dubbe, "Fundamentals of solid state ionic micro gas sensor", Sens. Actuat., 88 (2003) 138-148.

[3] B. Timmer, W. Olthuis and A. van den Berg, "Ammonia sensors and their applications - a review", Sen. Actuat., 107 (2005) 666-677.

[4] J. Gao et al., "Vapor sensors based on optical interferometry from oxidized microporous silicon films", Langmuir, 18 (2002) 2229-2233.

[5] M.A. Saidi, W.A. Rahman and R. Majid, "Effect of different solvents on the thermal, IR spectroscopy and morphological properties of solution casted PLA/starch films", Malaysian J. Fund. Appl. Sci., 10 (2014) 33-36.

[6] M.N.T. Seiyama, A. Kato and K. Fukushi, "A New Detector for Gaseous Components Using Semi conductive Thin Films", Anal. Chem, 34 (1996) 1502-1503.

[7] D.E. Williams, "Semiconducting oxides as gas-sensitive resistors", Sen. Actuat. B, 57(1) (1999) 1-16.

[8] B. Licznerski, "Thick-film gas microsensors based on tin dioxide", Bull. Polish Acad. Sci. Tech. Sci., 52 (2004) 37-42.

[9] L.A. Patil et al., "Synthesis of ZnO nanocrystalline powder from ultrasonic atomization technique, characterization, and its application in gas sensing", IEEE Sens. J., 11 (2011) 939-946.

[10] A.J. Mohammed, "Effect of molarity on the physical and sensing properties of ZnO thin

films prepared by spray pyolysis technique", University of Technology, Iraq, 2007.
[11] D.R. Patil et al., "Surface activated ZnO thick film resistors for LPG gas sensing", Sen. Transd. J., 74(12) (2006) 874-883.
[12] V.E. Bochenkov and G.B. Sergeev, "Sensitivity, Selectivity and Stability of Gas-Sensitive Metal-Oxide Nanostructures", Metal. Oxide Nanostr. Appl., 3 (2010) 31-52.
[13] G.W. Lu, L.T. Qu and G.Q. Shi, "Electrochemical fabrication of neuron-type networks based on crystalline oligopyrene nanosheets", Electrochem. Acta, 51 (2005) 340-346.
[14] B.J. Samuel (Editor), "Nanoporous Materials - Types, Properties and Uses", Nova Scientific Publishers, Inc. (NY, 2010).
[15] N. Barsan, M. Schweizer-Berberich and W. Gpel, "Fundamental and practical aspects in the design of nanoscaled SnO_2 gas sensors: a status report", Fresenius' J. Anal. Chem., 365(4) (1999) 287-304.
[16] J. Ramírez, X. Vilanova and E. Llobet, "Drop-coated sensing layer on ultra-low power hotplates for an RFID flexible tag microlab", Sen. Actuat. B, 144 (2010) 462-466.
[17] R. Tongpool and S. Yoriya, "Kinetics of nitrogen dioxide exposure in lead phthalocyanine sensors", Thin Solid Films, 477 (2005) 148-152.
[18] D. Meyerhofer, "Characteristics of resist films produced by spinning", J. Appl. Phys, 49 (1978) 3993.
[19] S. Günes and N.S. Sariciftci, "Efficient polysulfide electrolyte for CdS quantum dot-sensitized solar cell", Inorg. Chem. Acta, 185(1) (2008) 584-588.
[20] U. Nayef, "Fabrication and Characteristics of Porous Silicon for Photoconversion", Int. J. Basic Appl. Sci., 13(2) (2013) 61.
[21] K. Šalucha and A.J. Marcinkevičius, "Investigation of porous silicon layers as passivation coatings for high voltage silicon device", Electron. Electr. Eng., 79 (2007) 41-44.
[22] Ş. Doğan et al., "Porous Silicon: Volume-Specific Surface Area Determination from AFM Measurement Data", J. Mater. Sci. Eng. B, 3(8) (2013) 518-523.
[23] H. Saha, J. Das and S.M. Hossain, "Gas sensitive porous silicon devices: responses to organic vapors", Asian J. Phys., 93(1) (2003) 384-390.
[24] L. Wang et al., "Metal Oxide Gas Sensors: Sensitivity and Influencing Factors", Sensors, 10(3) (2010) 2088-2106.
[25] K. Albert et al., "Crossreactive chemical sensor arrays", Chem. Rev., 100(7) (2000) 2595-2626.
[26] K. Arshak et al., "A review of "gas sensors employed in electronic nose applications", Sen. Rev., 24(2) (2004) 181-198.
[27] P. Urbánek et al., "Thickness threshold of structural ordering in thin MEH-PPV films", Polymer, 55(16) (2014) 4050-4056.
[28] A. Guadarrama et al., "Array of conducting polymer sensors for the characterization of wines", Anal. Chem. Acta, 411(2) (2000) 193-200.

IRAQI JOURNAL OF APPLIED PHYSICS
Vol. 17, No. 3, July-September 2021, pp. 27-30

Thermogravimetric Properties of Porcelain Supported by Addition of Beryllium Oxide

Alireza Shahidi
Sardar Najafpur
Mahmood J. Abbasi
Fatema Asghari

Department of Mechanical Engineering,
College of Engineering,
University of Esfahan,
Esfahan, IRAN

Due to its specific characteristic of porcelain, specific recipes have been prepared. The basic materials and quantities were selected carefully because it possesses particular specifications. In this work, porcelain containing 32 wt.% feldspar, 24 wt.% quartz and 44 wt.% clay was synthesized. Different melting temperature (1300°C, 1375 °C and 1450°C) and insertion of beryllium oxide (BeO) (1, 3, 5 and 7 wt.%) were done. The effects of temperatures and beryllium oxide content on mechanical, electrical and structural properties on the prepared porcelain were studied. The increasing of heat treatment for the basic porcelain leads to an enhancement in bulk density and compressive strength. Basic porcelain which suffering lower annealing temperature (1300°C) introduces higher dielectric constant values in contrast with that suffering higher temperature (1450°C). The addition of BeO to the basic porcelain leads to decrease the bulk density and compressive strength. Porcelain with lower annealing temperature introduces higher ε values in contrast with higher temperature.

***Keywords*:** Beryllium oxide; Porcelain; Thermogravimetric; Green density

1. Introduction

Porcelain was used as an electrical insulating material due to its characteristic properties (mechanical and high-power dielectric strength, and corrosion resistance). Two types of porcelain insulators are mostly used: silica and alumina porcelains [1-3]. Since long time, Porcelain refers to a wide range of ceramic products baked at high temperatures to achieve vitreous, or glassy, qualities such as translucence and low porosity [1]. Porcelain was first made by the Chinese and the two natural substances used were kaolin and feldspar. The caolin is also known as china clay, which is white, free of impurities and melts at very high temperatures, while feldspar is mineral forming glassy cement and binding the vessel permanently [2].

The properties of porcelain are greatly varying from a source to another; however, many variations are not critical in resin composites [4]. Silicate materials, such as feldspar and kaolin, have alternating structure of the oxygen and silicon atoms in covalent bonding forming tetrahedral units [5]. Several processes, such as the destruction of dehydroxylation, ceramic lattice, destruction of the network, partial melting to form new phases, occur on silicate heating layer [4,5].

Amongst known oxides, beryllium oxide (BeO) combines excellent electrical insulation with high thermal conductivity [6]. It is one of the most chemically stable oxides, resisting both carbon reduction and molten metal attack at high temperatures. It also has high electrical resistivity and low density [5-7]. Also, it has low dielectric constant of 6.7 and low loss index of 0.0012 at 1 MHz, which mean the increases in losses index with increasing of applied frequency [8]. Furthermore, BeO is inherently stable, as an oxide ceramic, in oxygen and moisture-containing environments [8-10]. The most common and economically important system is the $BeO\text{-}Al_2O\text{-}SiO_2\text{-}H_2O$ (BASH) [11].

The layer stacking of kaolinite is controlled by repulsion between highly charged Si and Al cations, which tend to avoid superposition. Unfortunately these functional groups are equally present in several other aluminosilicates [12]. The Si-O, Al-O and OH play functional roles in identification and characterization for chemical composition of a kaolinite unit cell [13-15].

2. Experimental Part

The starting materials used to prepare the basic porcelain include 32 wt% feldspar, 24 wt% quartz, and 44 wt% clay. After selecting raw materials, the desired amounts were weighed then sent through a series of preparation steps. First, they are crushed and purified, before mixed together and subjected to pressing forming process. The raw material particles were reduced to the desired size by sieving with mesh equal to 53μm. For fine grinding, ball mill for 1 hour consisting of rotating cylinder partially filled with spherical ceramic grinding media was used. Beryllium oxide was introduced at four different amounts; 1, 3, 5 and 7wt%.

Samples of about 50g were melted in a furnace at temperatures of 1300, 1375 and 1450°C, and heating time of 90 min. Then the basic and different BeO

content porcelain samples were "quenched" to room temperature at ambient conditions to avoid crystallization of amorphous metakaolin. Samples were prepared by weighing of 2g then pressing as a disk shape with 1.5 cm in diameter. In order to eliminate the stresses that accompany the milling operation, heat treatment process was performed at 950°C. During the firing process, a variety of reactions take place. First, carbon-based impurities burn out, chemical water evolves (at 100 to 200°C), and carbonates and sulfates begin to decompose (at 400 to 700°C) lead gases to be produced and escape from the sample. On further heating, some of the minerals break down into other phases, and the present fluxes (feldspar and flint) react with the decomposing minerals to form liquid glasses at 700 to 1100°C. These glass phases are necessary for shrinking and bonding the grains. After the desired density is achieved at higher than 1200°C, the ware is cooled, which causes the liquid glass to solidify, thereby forming a strong bond between the remaining crystalline grains, and finally, the porcelain is completed.

This is the first time that the influence of addition of BeO to the basic porcelain were studied.

Prepared samples were subjected to green density, bulk density, and compressive strength tests. The AC conductivity of the samples containing 3 and 7wt% BeO were chosen for measurement to clarify the ratios difference.

3. Results and Discussion

The variation of BeO content relative to the green density (G.D) is shown in Fig. (1). The addition of small amount of BeO into basic porcelain leads initially to slowly decrease in G.D., addition of more BeO percentage causes to clearly decrease in G.D. In other words, the additions of 1 and 3wt% of BeO have the same effects and the densification process is in its initial stage. So, at these percentages, the BeO addition does not improve the densification process. Increasing the BeO content to more than 3wt.% leads to decreases the samples density. It can be expected that increasing of BeO introduces more voids among the particles, which produce a large volume with less dense material, or it is possible attributed to the increasing of BeO which possess low-density.

In order to provide clear information about the influence of temperature, 1300 °C and 1450 °C has been chosen for bulk density, compressive strength, AC conductivity and FTIR tests. Also, specific percentages of 3 and 7% BeO were chosen to supply for the same tests. Figure (2) shows the influence of heat treatment on the basic and new-composed porcelains. The basic porcelain has little enhancement in bulk density with increasing heat treatment, which means that increasing temperature leads to voids elimination and produce close particles, i.e., the volume of material is affected by decreasing linear shrinkage due to the movement of particles into the pores. This leads to densification and decrease in the porosity of the ceramic body. At 1450°C, the sintering is significantly improved and the transformation of open-into-closed porosity is expected.

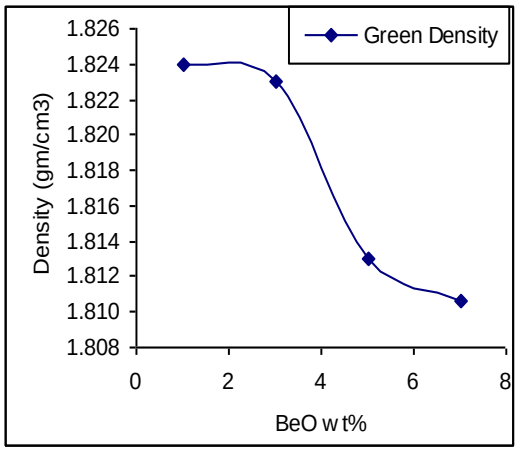

Fig. (1) The variation of green density according to BeO wt.% addition

Samples containing 3 and 7wt% BeO provide approximately equal values of bulk density at 1300 and 1375°C. Increasing treatment temperature to 1450°C leads to less dense material. Samples containing higher contents of BeO exhibit lower densities in contrast to those containing smaller contents. This behavior can be attributed to the formation of new phases due to increasing concentration of BeO powder in each addition with assistance of temperature. Figure (2) clearly revealed this behavior at different BeO contents.

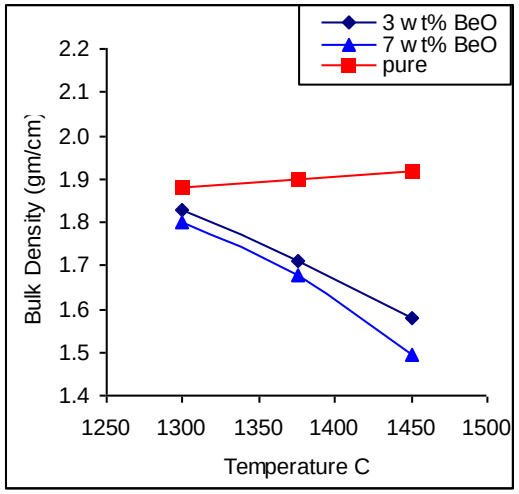

Fig. (2) The variation of bulk density for basic and new porcelain versus temperatures

The dependence of compressive strength for basic and addition BeO porcelains at different treatment temperatures is shown in Fig. (3). It is observed that the basic has higher compressive strength, and increasing temperature leads to increase compressive strength. When the sintering temperature was raised

to 1450°C, the molten part of the component starts to participate in the dissolution of the quartz phase and enhance the densification process. As a result, the sintering was improved and products with lower porosity and higher mechanical properties were obtained. This result was in agreement with that obtained from bulk density (dense materials produce higher strength). Samples containing less BeO show highly compressive strength at 1300°C than those treated at 1450°C. Increasing BeO content and treatment temperature leads to low strength material.

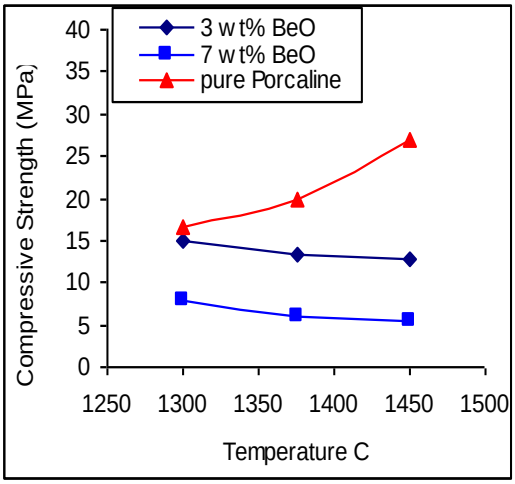

Fig. (3) Compressive strength as a function of heat treatment

The variation of frequency-dependent dielectric constant (έ) for basic porcelain and porcelain containing different BeO contents at different temperatures (1300 and 1450°C) was shown in Fig. (4). All samples revealed slightly decrease in dielectric constant at lower applied field 40 Hz to 200 kHz, and then show stable values in spite of increasing applied frequency. A comparison between the basic and new-composed porcelains revealed high value of dielectric constant for the basic porcelain with respect to those containing 3 and 7 wt.% BeO.

Porcelain with a lower annealing temperature (1300°C) produce higher έ values in contrast with higher temperature (1450°C). This result was also recorded for the porcelain samples containing 3 and 7 wt.% BeO. The composition of the basic porcelain, which has high quantities of SiO_2 (24wt% knowing as quartz), introduces material with high dielectric constant. Increasing treatment temperature leads to destroy Si-O-Si bonds and then formation of new composition with lower έ values.

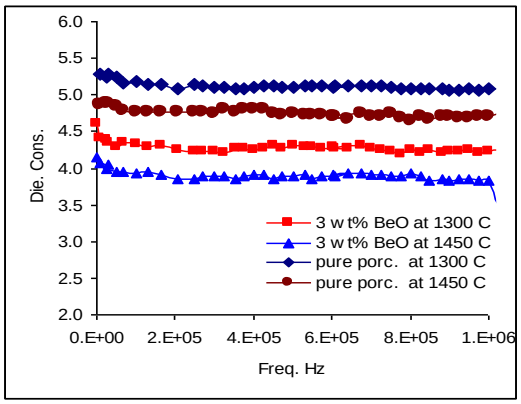

(a)

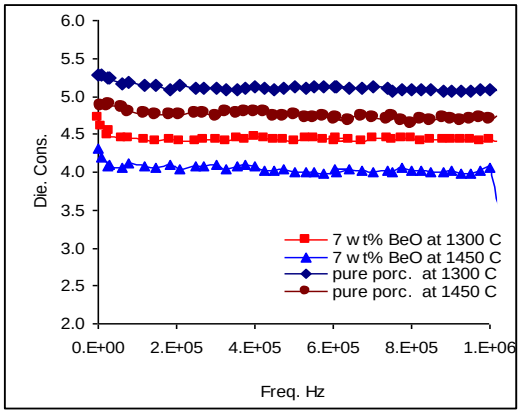

(b)

Fig. (4) The dependence of dielectric constant for pure porcelain and addition 3% and 7% of BeO to it at different heat treatment

Figure (5) shows the relation between the dielectric losses or dissipation factor (ε″) and applied frequency for basic porcelain and porcelains containing 3 and 7 wt.% BeO. Increasing frequency leads to pronounced decreasing in ε″ within frequency range 40 Hz to 300 kHz. As well, increasing frequency for prepared samples shows linearly stable values of dielectric losses. Sample containing 7 wt.% BeO and subjected to 1300°C heat treatment revealed higher dielectric losses than that containing 3 wt.% BeO at the same conditions.

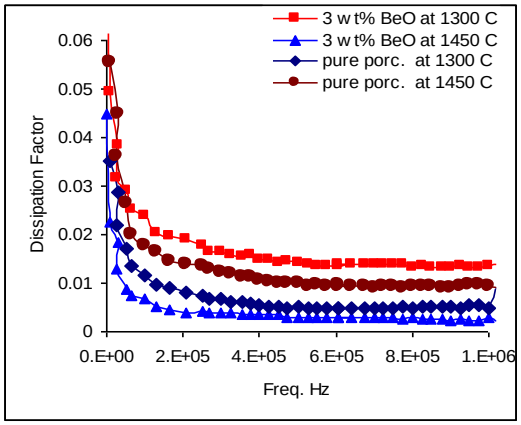

(a)

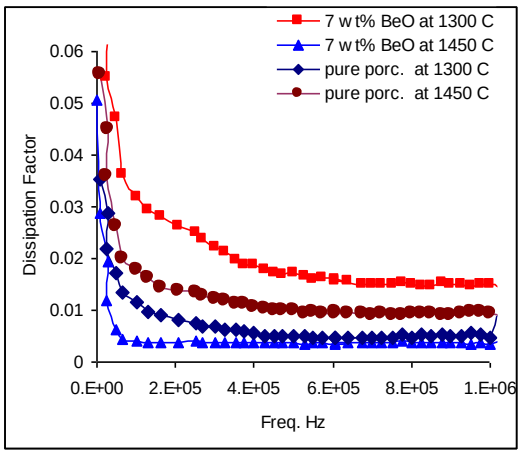

(b)

Fig. (5) The dependence of dielectric losses for pure porcelain and addition 3% and 7% of BeO to it at different heat treatment

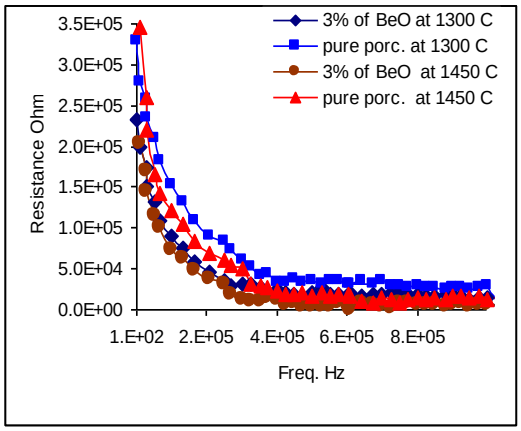

(a)

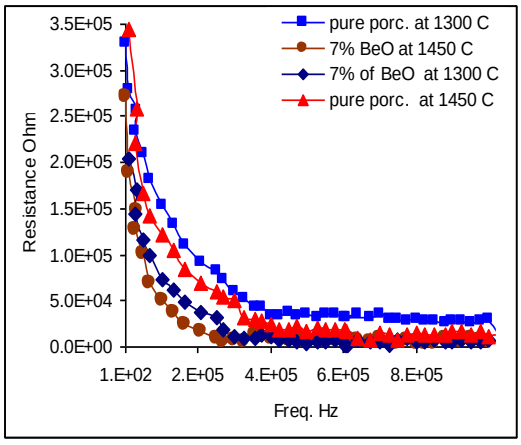

(b)

Fig. (6) The variation of resistance for pure porcelain and addition 3% and 7% of BeO to it at different heat treatment

4. Conclusion

Increasing treatment temperature of basic porcelain enhances the bulk density, compressive strength and dielectric properties. In contrast, increasing the BeO content in the porcelain causes to degrade the properties mentioned above. In all prepared samples, the octahedral sheet has changed into tetrahedral of metakaolin at calcination temperatures of 1300 and 1450°C, which was confirmed by the FTIR spectroscopy. The properties of porcelain can be enhancing by controlling the fractional content of BeO as well as the treatment temperature of the composition.

References

[1] N. Shashidhar and J.S. Reed, "Recycling Fired Porcelain", Ceram. Bull., 69(5) (1990) 834-841.

[2] M.W. Carty and U. Senapati, "Porcelain-raw materials, processing, phase evolution, and mechanical behavior", J. Am. Ceram. Soc., 81(1) (1998) 3-21.

[3] S. Valenstein, **"A Handbook of Chinese Ceramics"**, 1989.

[4] M. Dawy, "Electrical Properties and Infrared Studies of Heated Mica Sheets", Egypt. J. Sol., 25(1) (2002).

[5] X.C. Tong, "Technology and Engineering Advanced Materials for Thermal Management of Electronic Packaging", PhD Springer Science & Business Media, Jan 5, 2011.

[6] J.L. Sepulveda and L.J. Vandermark, "High Thermal Dissipation Ceramics and Composite Materials for Microelectronic Packaging", 2010, pp. 207-232.

[7] S. Braganca and C. Bergmann, "Waste Glass in Porcelain", Mater. Res., 8(1) (2005) 39-44.

[8] S. Yürüyen and H. Özkan Toplan, "The sintering kinetics of porcelain bodies made from waste glass and fly ash", Ceram. Int., 35(6) (2009) 2427-2433.

[9] N. Shashidhar and J.S. Reed, "Recycling Fired Porcelain", Ceram. Bull., 69(5) (1990) 834-841.

[10] R.A. Condrate Sr, "The Infrared and Raman Spectra of Glasses, Introduction to Glass Science", 1972, pp. 101-135.

[11] A. Hölscher, W. Schreyer and D. Lattard, "High-pressure, high-temperature stability of surinamite in the system MgO-BeO-Al_2O_3-SiO_2-H_2O", Contrib. to Miner. Petrol., 92(1) (1986) 113-127.

[12] G.E. Ekosse, "Fourier Transform Infrared Spectrophotometry and X-ray powder Diffractometry as Complementary Techniques in characterizing Clay size fraction of Kaolin", J. Appl. Sci. Environ. Mgt., 9(2) (2005) 43-48.

[13] J.B. Dixon, **"Minerals in the environment"**, 2nd ed. SSSA Book Series No.1 (1989) 467-523.

[14] B. Lanson et al., "Authigenic kaolin and illitic minerals during burial diagenesis of sandstones: a review", Clay Miner., 37 (2002) 1-22.

[15] C. Belver, M.A.B. Munoz and M.A. Vicente, "Chemical activation of a kaolinite under acid and alkaline condition", Chem. Mater., 14 (2002) 2033-2043.

THE IRAQI JOURNAL OF APPLIED PHYSICS
EDITORIAL BOARD

COPYRIGHT RELEASE FORM
IRAQI JOURNAL OF APPLIED PHYSICS (IJAP)

We, the undersigned, the author/authors of the article titled

……
……
……
……
……
……
……

that is submitted to the Iraqi Journal of Applied Physics (IJAP) for publication, declare that we have neither taken part or full text from any published work by others, nor presented or published it elsewhere in any other journal. We also declare transferring copyrights and conduct of this article to the Iraqi Journal of Applied Physics (IJAP) after accepting it for publication.

The authors will keep the following rights:

1. Possession of the article such as patent rights.
2. Free of charge use of the article or part of it in any future work by the authors such as books and lecture notes after informing IJAP editorial board.
3. Republishing the article for any personal purposes of the authors after taking journal permission.

To be signed by all authors:

Signature:……..date: ……
Printed name: ……

Signature:……..date: ……
Printed name: ……

Signature:……..date: ……
Printed name: ……

Correspondence
address:……...
……
Address:……
……
Telephone:……..……email: ……

Note: Complete and sign this form and mail it to the below address with your finally revised manuscript

The Iraqi Journal of Applied Physics
www.iraqiphysicsjournal.com
Email: info@iraqiphysicsjournal.com
Email: editor_ijap@yahoo.co.uk
Email: irq_appl_phys@yahoo.com

IRAQI JOURNAL OF APPLIED PHYSICS

Volume (17), Issue (3), July-September 2021

CONTENTS